



NKS-264  
ISBN 978-87-7893-337-9

---

# Modeling of interaction of multiple vent pipes in a pressure suppression pool

Antti Timperi  
Michael Chauhan  
Timo Pättikangas  
Jarto Niemi

VTT - Technical Research Centre of Finland

April 2012

## Abstract

Calculations of direct-contact condensation in the pressure suppression pool have been performed. Partial pressure model for the condensation of pure vapor is used for the condensation, which makes possible modeling of the condensation of pure vapor. The heat and mass transfer during condensation is studied in detail for experiment PAR-10 in the PPOOLEX facility.

The rapid collapse of a steam bubble in PPOOLEX experiment COL-01 has been analyzed with the new Eulerian model of Abaqus. By observing the collapse behavior, the pressure variation inside the bubble was fitted with the experiment. The effect of system size on the pressure peak was also examined; these results can be used for studying more thoroughly the scaling of the experimental results to full-scale in future.

The desynchronization of chugging events in the two vent experiment PAR-10 was studied. The statistical distribution of desynchronization was determined from the measured pressure data and compared to results obtained in a seven vent pipe experiment found from literature. The response of BWR containment during desynchronized chugging events and with varying speeds of sound was numerically computed using direct time integration and modal dynamics procedure available in Abaqus.

## Key words

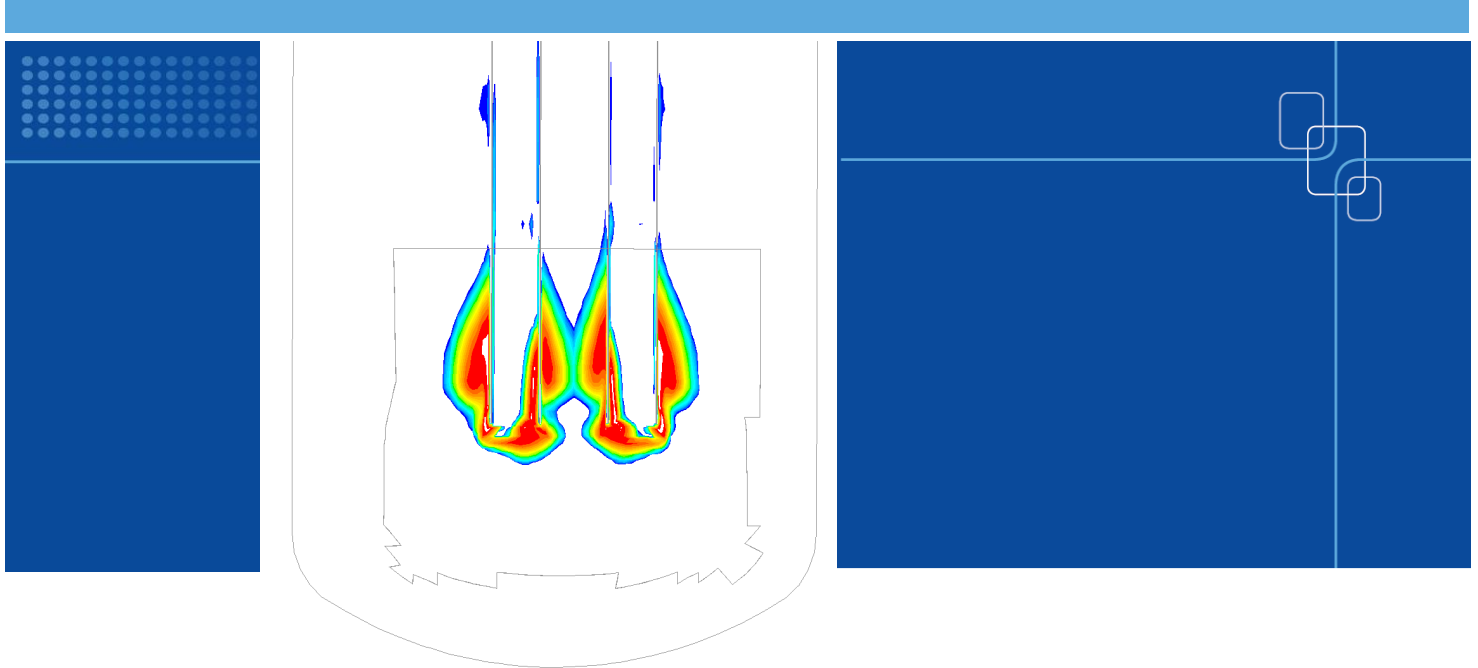
Condensation pool, pressure suppression pool, BWR, CFD, fluid-structure interaction, FSI

NKS-264  
ISBN 978-87-7893-337-9

Electronic report, April 2012

NKS Secretariat  
P.O. Box 49  
DK - 4000 Roskilde, Denmark




Phone +45 4677 4041  
[www.nks.org](http://www.nks.org)  
e-mail [nks@nks.org](mailto:nks@nks.org)



## Modeling of Interaction of Multiple Vent Pipes in a Pressure Suppression Pool

Authors: Antti Timperi, Michael Chauhan, Timo Pättikangas and Jarto Niemi  
Confidentiality: Public



Report's title		
Modeling of interaction of multiple vent pipes in a pressure suppression pool		
Customer, contact person, address		Order reference
1. Valtion ydinjäterahasto, Työ- ja elinkeinoministeriö, PL 32, 00023 VALTIONEUVOSTO		1. SAFIR2014 Programme: Dnro 19/2011SAF
2. Nordic nuclear safety research (NKS) c/o Fortum Power and Heat Oy, Karoliina Myllymäki, PL 100, 00048 FORTUM		2. NKS Contract no. AFT/NKS-R(11)90/3
Project name		Project number/Short name
Numerical modeling of condensation pool		73416 / NUMPOOL2011
Author(s)		Pages
Antti Timperi, Michael Chauhan, Timo Pättikangas and Jarto Niemi		54
Keywords		Report identification code
Condensation pool, pressure suppression pool, BWR, CFD, fluid-structure interaction, FSI		VTT-R-01094-12
Summary		
<p>Calculations of direct-contact condensation in the pressure suppression pool have been performed. Partial pressure model for the condensation of pure vapor is used for the condensation, which makes possible modeling of the condensation of pure vapor without any non-condensable gas. Numerical diffusion is reduced near the vent outlets by using several methods. The heat and mass transfer during condensation is studied in detail for experiment PAR-10 in the PPOOLEX facility.</p> <p>The rapid collapse of a steam bubble in PPOOLEX experiment COL-01 has been analyzed with the new Eulerian model of Abaqus. By observing the collapse behavior, the pressure variation inside the bubble was fitted with the experiment. The pressure variation can be used for estimating the condensation rate of steam in future. The effect of system size on the pressure peak was also examined; these results can be used for studying more thoroughly the scaling of the experimental results to full-scale in future.</p> <p>The desynchronization of chugging events in the two vent experiment PAR-10 was studied. The statistical distribution of desynchronization was determined from the measured pressure data and compared to results obtained in a seven vent pipe experiment found from literature. The response of BWR containment during desynchronized chugging events and with varying speeds of sound was numerically computed using direct time integration and modal dynamics procedure available in Abaqus. The preliminary results show significant decrease in the loads experienced by the containment, when the desynchronization is taken into account.</p>		
Confidentiality	Public	
Espoo, 23.3.2012		
Written by	Reviewed by	Accepted by
		
Antti Timperi, Senior Scientist	Arja Saarenheimo, Principal Scientist	Eila Lehmus, Technology Manager
VTT's contact address		
VTT Technical Research Centre of Finland, P.O.B. 1000, FI-02044 VTT, Finland		
Distribution (customer and VTT)		
Karoliina Ekström (NKS), STUK, Timo Toppila (Fortum), Vesa Suolanen (VTT), Pavel Kudinov (KTH), Vesa Tanskanen (LUT), Markku Puustinen (LUT), Heikki Purhonen (LUT), Jani Laine (LUT), SAFIR2014 Reference Group 4		
<p><i>The use of the name of the VTT Technical Research Centre of Finland (VTT) in advertising or publication in part of this report is only permissible with written authorization from the VTT Technical Research Centre of Finland.</i></p>		

## Preface

This work has been carried out in the NUMPOOL project of the SAFIR2014 programme (The Finnish Research Programme on Nuclear Power Plant Safety). The project has been funded by Valtion ydinjäterahasto, VTT and NKS (Nordic nuclear safety research). The authors are grateful for comments obtained from the members of the SAFIR2010 Reference Group 4 and from the Northnet Roadmap 3 Reference Group.

Espoo 23.3.2012

Authors

## Contents

Preface .....	2
1 Introduction.....	4
2 CFD modeling of chugging .....	5
2.1 PPOOLEX experiment PAR-10.....	5
2.2 CFD model for the experiments with two vent pipes .....	5
2.3 Condensation model based on partial pressure of steam .....	8
2.4 Simulation results.....	9
3 Pressure loads due to collapsing vapor bubble .....	16
3.1 Analysis of experiment COL-01 .....	16
3.2 Eulerian FEM calculations.....	23
3.2.1 Comparison of 1D and 2D models .....	23
3.2.2 Comparison of spherical and toroidal bubbles .....	25
3.2.3 Modeling of the PPOOLEX facility .....	31
4 Analysis of the desynchronization of bubble collapses.....	36
4.1 Comparison between visual observations and measured pressures .....	36
4.2 Desynchronization of chugging between two vent pipes.....	39
4.3 Comparison between earlier experiments.....	41
5 Preliminary FEM calculations of chugging in a BWR containment .....	42
5.1 Acoustic-structural analysis.....	42
5.2 Load description.....	44
5.3 Results and discussion .....	48
6 Discussion .....	51
References .....	53

## 1 Introduction

In boiling water reactors (BWR), the major function of the containment system is to protect the environment if a loss-of-coolant accident (LOCA) should occur. The containment is designed to accommodate the loads generated in hypothetical accidents, such as sudden rupture of a main steam line. In such an accident, a large amount of steam is suddenly released in the containment. An essential part of the pressure suppression containment is a water pool, where condensation of released steam occurs.

In a BWR, the pressure suppression containment typically consists of a drywell and a wetwell with a water pool. In a hypothetical LOCA, steam and air flow from the drywell through vent pipes to the wetwell, where the outlets of the vent pipes are submerged in the water pool. In the early part of the accident, mainly non-condensable air or nitrogen flows through the vent pipes into the wetwell. Then, the volume fraction of vapor increases in the gas mixture. When all the non-condensable gas from the drywell has been blown into the wetwell, the blowdown consists of pure vapor. At this stage, so-called chugging effect may occur, which means periodic formation and rapid condensation of large vapor bubbles at the vent outlets (Lahey and Moody, 1993). The rapid condensation of the vapor bubbles may induce significant pressure loads on the structures in the pressure suppression pool and on the containment.

In the present work, a computational fluid dynamics (CFD) simulation of chugging is performed by using the Euler-Euler two-phase model of the commercial Fluent code. An experiment performed with the PPOOLEX facility by Puustinen et al. (2011) at the Lappeenranta University of Technology is modeled. The direct-contact condensation in the water pool is modeled with user-defined functions implemented in the Fluent code.

The rapid collapse of a vapor bubble and the pressure loads are also modeled by using the Abaqus finite element method (FEM) code (Abaqus, 2011). The new Eulerian method of Abaqus is used for calculating the bubble collapse by taking into account the toroidal shape of the bubble, the vent pipe and the finite pool geometry. The effect of various parameters, such as system dimensions, on the pressure load are first studied for the cases of spherical and toroidal bubbles. Calculations are then performed for the PPOOLEX experiment COL-01, where fairly large pressure loads were measured. Bubble collapses giving the largest pressure loads in the experiment are analyzed and the calculated collapse times and pressure loads are compared with the experiment.

The pressure suppression pools of BWRs have typically a large number of vent pipes. Experiments have shown that the pressure loads originating from different vent pipes are slightly desynchronized (Kukita and Namatame, 1985; Puustinen et al., 2011). The desynchronization reduces the overall pressure load compared to fully synchronous chugging at all vent pipes. The experimental results for desynchronization are studied and applied to a model of a BWR containment.



## 2 CFD modeling of chugging

The PPOOLEX experiment PAR-10 was used as a test for the modifications of the CFD model for direct-contact condensation. Several modifications were made compared to the earlier calculations (Pättikangas et al., 2011). In the following, we first briefly describe the experiment PAR-10. Second, we discuss the changes made in the modeling since the previous calculations. Third, we describe in detail the condensation model used in the present calculations. Finally, the CFD simulation results are presented and discussed.

### 2.1 PPOOLEX experiment PAR-10

The PPOOLEX facility is a pressurized cylindrical vessel with a height of 7.45 meters and a diameter of 2.4 meters. The volume of the drywell compartment is 13.3 m<sup>3</sup> and the volume of the wetwell compartment is 17.8 m<sup>3</sup>. Steam is blown into the drywell compartment via a horizontal DN200 inlet plenum. The experimental facility has earlier been described in detail by Puustinen, Laine and Räsänen (2010).

In 2010, PAR-10 experiment was performed, where the interaction of two parallel vent pipes was studied. In the following, we concentrate on the time interval  $t = 500 \dots 600$  s of the experiment when chugging was found to occur.

The CFD calculation was carefully initialized to correspond to the situation at time  $t = 500$  s. It was assumed that the amount of non-condensable gas in the drywell was very small because almost all air had already been blown to the wetwell. The mole fraction of air in the drywell was assumed to be 0.01 %. The temperature of the gas in the drywell was 140 °C. Since the drywell was insulated, the walls were initialized to the same temperature. The pressure in the drywell was  $p_{DW} = 2.89$  bar.

The temperature of the water pool was 43 °C. The temperature of the gas space of the wetwell was stratified such that a linear temperature profile between 33 °C and 61 °C was used in the initialization.

The mass flow rate of vapor from the inlet plenum to the drywell was 0.523 kg/s and it was kept constant during the calculation. The temperature of the vapor was 155 °C and it contained a mass fraction of 0.01% of air. According to the chugging maps presented by Lahey and Moody (1993), the experiment is in the chugging region. This was verified by experimental observation in the experiment PAR-10.

### 2.2 CFD model for the experiments with two vent pipes

The surface mesh of the CFD model prepared for the PPOOLEX facility with two vent pipes is shown in Figure 1. The horizontal inlet plenum and the drywell and wetwell compartments can be seen of the left-hand side. Two vertical vent pipes from the drywell compartment to the water pool of the wetwell compartment can also be seen. In order to reduce numerical diffusion, the mesh was adapted in the region around the vent outlets, where the direct-contact condensation occurs.

Details of the resulting finer mesh are shown on the right-hand side in Figure 1, where the mesh around the vent pipes is shown. The adaption increased the number of the mesh cells from 180 000 to 275 000.

The CFD calculations were performed by using the Euler-Euler two-phase model of Fluent 13.0. The Euler-Euler model is a two-fluid model, where conservation of mass, momentum and energy are solved for gas and liquid water. The gas phase consisted of two species components: dry air and vapor.

The treatment of non-condensable gas was changed compared to the previous modeling attempts (Pättikangas et al., 2011). First, the mass fraction of non-condensable gas flowing into the drywell was reduced from 1 % to 0.01 % because enrichment of the non-condensable gas occurs in the vent pipes. Already 1...2 % of non-condensable gas may prevent chugging. The mixture of the gases was treated as a compressible ideal gas. The floating operating pressure option of Fluent was used for modeling the increasing pressure inside the vessel.

In the earlier calculations, turbulence was modeled with the standard  $k-\varepsilon$  model for the mixture of the phases. This model was found to produce fairly large values of turbulent viscosity, which may be one reason for the very synchronous behavior of the two vent pipes. In the present simulations, the re-normalization group (RNG)  $k-\varepsilon$  model for the mixture is used because it is expected to produce smaller values of turbulent viscosity.

In the present calculations, the amount of non-condensable gas is very small. Therefore, the previously used condensation model is not feasible because it was based on diffusion of steam through non-condensable gas. Instead, a model based on partial pressure of steam in the mixture was used, which is described in detail in the next section.

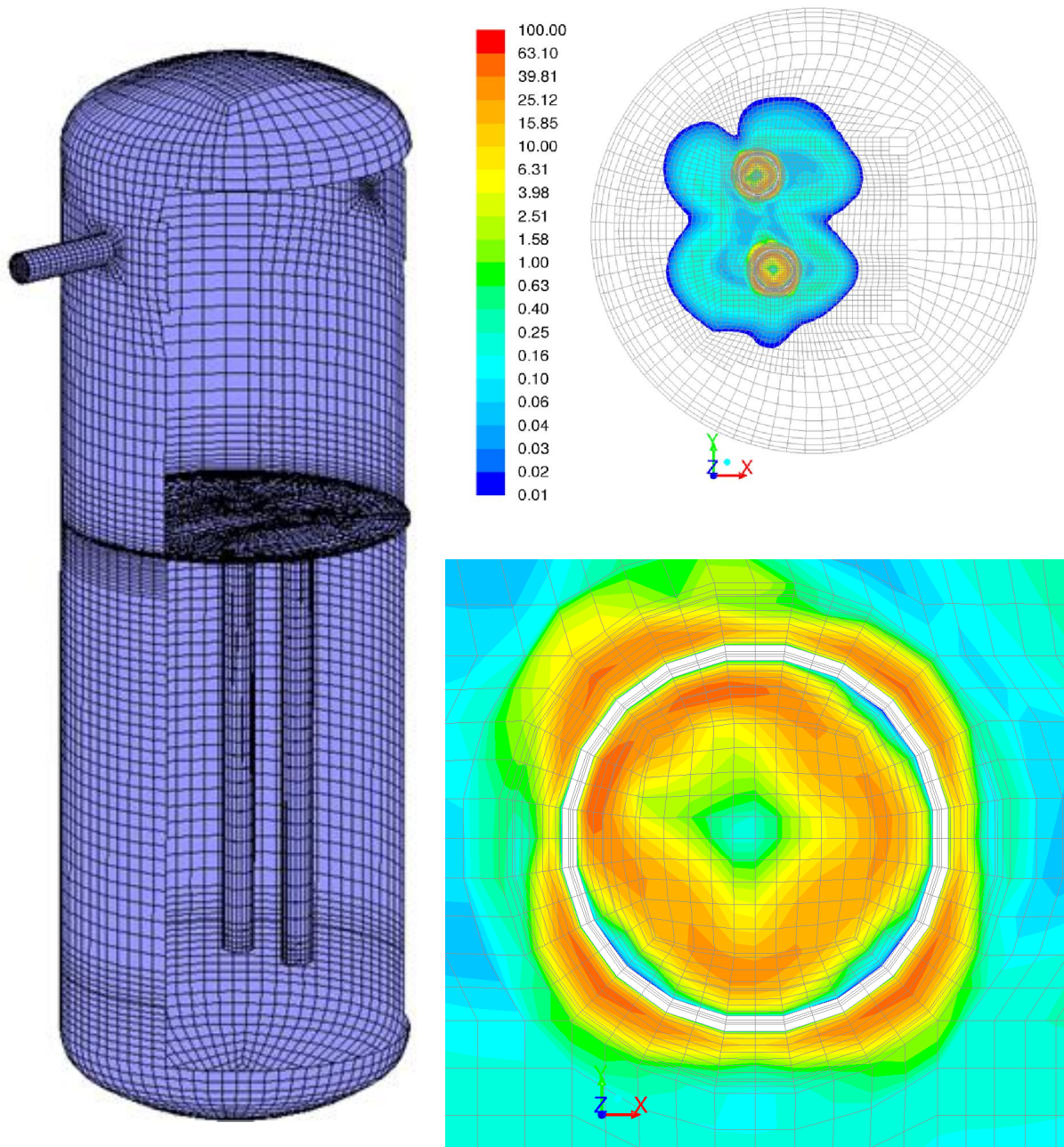


Figure 1. Surface mesh of the CFD model for the experiments with two vent pipes is shown on the left-hand side. On the right-hand side, the adapted finer mesh is shown in the horizontal plane near the outlet of the vent pipes. Details of the mesh are also shown near the outlet of one of the vent pipes (bottom right).

### 2.3 Condensation model based on partial pressure of steam

The model assumes that gas–water interactions take place in a thin massless interface layer between gas and water. Conceptually, the gas volume is divided into two parts. The first part contains the non-condensable gas and the second part contains the steam. Both parts share the same temperature  $T_{\text{gas}}$  and the sizes of the parts are determined by the mole fractions. The transition from steam to water is assumed to occur at the saturation temperature of the steam. The saturation temperature is determined at the partial pressure of the steam.

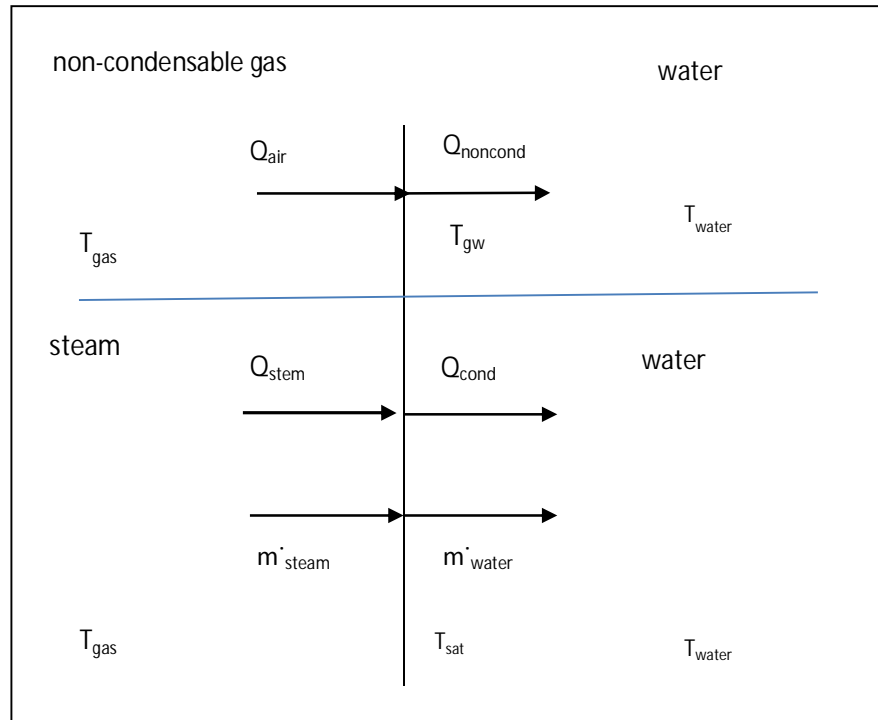


Figure 2. The mass and energy fluxes in condensation.

Consider first the energy balance of non-condensable gas and water. The heat flux is weighted by the mole fraction of the non-condensable gas:

$$Q_{\text{air}} = Q_{\text{noncond}} = y_{\text{noncond}} \frac{h_{\text{tc}_{\text{gas}}} h_{\text{tc}_{\text{water}}}}{h_{\text{tc}_{\text{gas}}} + h_{\text{tc}_{\text{water}}}} (T_{\text{gas}} - T_{\text{water}}) \quad (1)$$

In the mass balance of steam and water, the mass fluxes are always equal

$$\dot{m}_{\text{steam}} = \dot{m}_{\text{water}} \quad (2)$$

Condensation occurs, when the steam mass flux is positive and the energy balance is

$$Q_{\text{steam}} + \dot{m}_{\text{steam}} h_{\text{steam}}(T_{\text{gas}}) = Q_{\text{cond}} + \dot{m}_{\text{water}} h_{\text{water}}(T_{\text{sat}}) \quad (3a)$$

Evaporation occurs, when the mass flux is negative and the energy balance is

$$Q_{\text{steam}} + \dot{m}_{\text{steam}} h_{\text{steam}}(T_{\text{sat}}) = Q_{\text{cond}} + \dot{m}_{\text{water}} h_{\text{water}}(T_{\text{water}}) \quad (3b)$$

Steam heat flux is weighted by the mole fraction of steam:

$$Q_{\text{steam}} = y_{\text{steam}} h_{tc_{\text{gas}}} (T_{\text{gas}} - T_{\text{sat}}) \quad (4)$$

The corresponding water heat flux is

$$Q_{\text{cond}} = y_{\text{steam}} h_{tc_{\text{water}}} (T_{\text{sat}} - T_{\text{water}}) \quad (5)$$

The enthalpies can be estimated by

$$h_{\text{steam}}(T) = h_{\text{steam}}(T_{\text{sat}}) + C_{p,\text{steam}}(T - T_{\text{sat}}) \quad (6)$$

$$h_{\text{water}}(T) = h_{\text{water}}(T_{\text{sat}}) + C_{p,\text{water}}(T - T_{\text{sat}})$$

Equations (2)–(6) are combined and solved for the condensation mass flux:

$$\dot{m}_{\text{steam}} = \frac{Q_{\text{cond}} - Q_{\text{steam}}}{h_{\text{fg}} + C_{p,\text{steam}}(T_{\text{gas}} - T_{\text{sat}})} \quad (7)$$

In case of evaporation, the mass flux is

$$\dot{m}_{\text{steam}} = \frac{Q_{\text{cond}} - Q_{\text{steam}}}{h_{\text{fg}} - C_{p,\text{water}}(T_{\text{water}} - T_{\text{sat}})} \quad (8)$$

Here  $h_{\text{fg}}$  is the latent heat

$$h_{\text{fg}} = h_{\text{steam}}(T_{\text{sat}}) - h_{\text{water}}(T_{\text{sat}}) \quad (9)$$

The model of Hughes and Duffey (1991) based on the surface renewal theory of Banerjee (1978) was used for the heat transfer coefficient with modifications introduced by Coste et al. (2008). This model has recently been used, e.g., by Štrubelj et al. (2010) and by Tanskanen (2008). The model was described in detail by Pättikangas et al. (2011).

## 2.4 Simulation results

In the following, the results for the simulation of the experiment PAR-10 are discussed. The simulation was first initialized to the situation corresponding to the experiment at time  $t = 500$  s as was described in Sec. 2.2. We next investigate in detail the formation and the condensation of the vapor at the vent outlets at time interval  $t = 4.8 \dots 5.5$  s.

In Figure 3, the volume fraction of gas is shown during one chugging cycle. The gas contains almost pure vapor because only negligible amount of non-condensable gas is present. A vapor bubble is formed at the vent outlets at time  $t = 5.1$  s. Part of the vapor rises upwards and is condensed before reaching the water surface. Condensation continues at the vent outlets and some water is penetrating into the vent pipes.

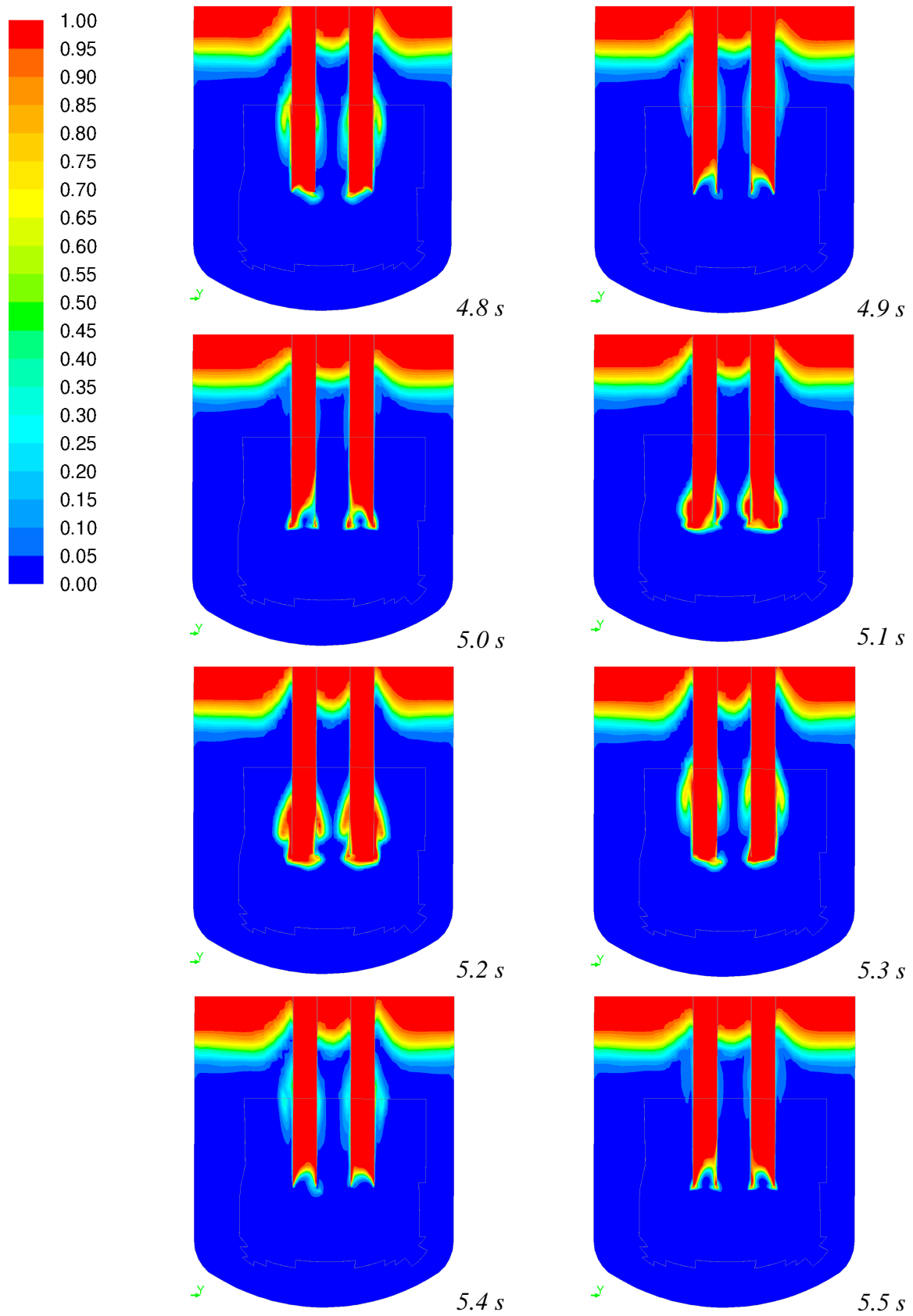


Figure 3. Volume fraction of gas at different instants of time during condensation of a gas bubble.



The heat transfer coefficient calculated from the Hughes-Duffey model is shown in Figure 4. The maximum values of the heat transfer coefficient are found at time  $t = 5.1 \dots 5.2$  s, when bubbles are formed at the vent outlet. The maximum values of the heat transfer coefficient in the present simulation are  $htc_{\text{water}} = 1 \dots 7 \text{ MW/m}^2\text{K}$ . Note that the values above the scale are not shown in Figure 4.

The interfacial area concentration is shown in Figure 5. The interfacial area concentration is estimated from the gradient of the void fraction. The maximum values are above  $20 \text{ m}^{-1}$  and they occur at the vent outlet, where the vapor bubbles are forming.

The volumetric heat transfer coefficient is obtained as the product of the heat transfer coefficient and the interfacial area concentration:  $htc_{\text{water}} \times a_i$ . The volumetric heat transfer coefficient is shown in Figure 6 on a logarithmic scale. In the present simulation, the maximum values at the vent outlets are above  $10 \text{ MW/m}^3\text{K}$ .

In Figure 7, the liquid generation rate from vapor in the direct contact condensation is shown. The maximum values are about  $15 \text{ kg/m}^3\text{s}$  near the vent outlets. Some condensation also occurs in the region above the vent outlets

Comparison of the numerical results to the PAR-10 experiment shows some clear differences. In the simulation, the period of chugging is much shorter than in the experiment. The period in the simulation is about 0.7 s and in the experiment about 1.7 s. In spite of the changes done in the modeling, the condensation is still too weak. In the experiment, all the condensation occurs near the outlet of the vent pipe or inside the vent pipe. On the contrary, in the simulation some condensation occurs in the vapor plume rising upwards from the vent outlet.

The differences between the simulation and the experiment are probably caused by three main reasons. First, the heat transfer coefficient between liquid water and vapor may still be too small. Second, the interfacial area estimated from the gradient of the void fraction is probably too small. The product of the heat transfer coefficient and the interfacial area determine the condensation rate, and it is difficult to distinguish their roles in the experimental result. Third, one can see in the experiment that mixing is rapidly increased on the interface of the vapor bubble when it starts collapsing at the vent outlet. The role of this increased mixing is still not properly taken into account in the present numerical model.

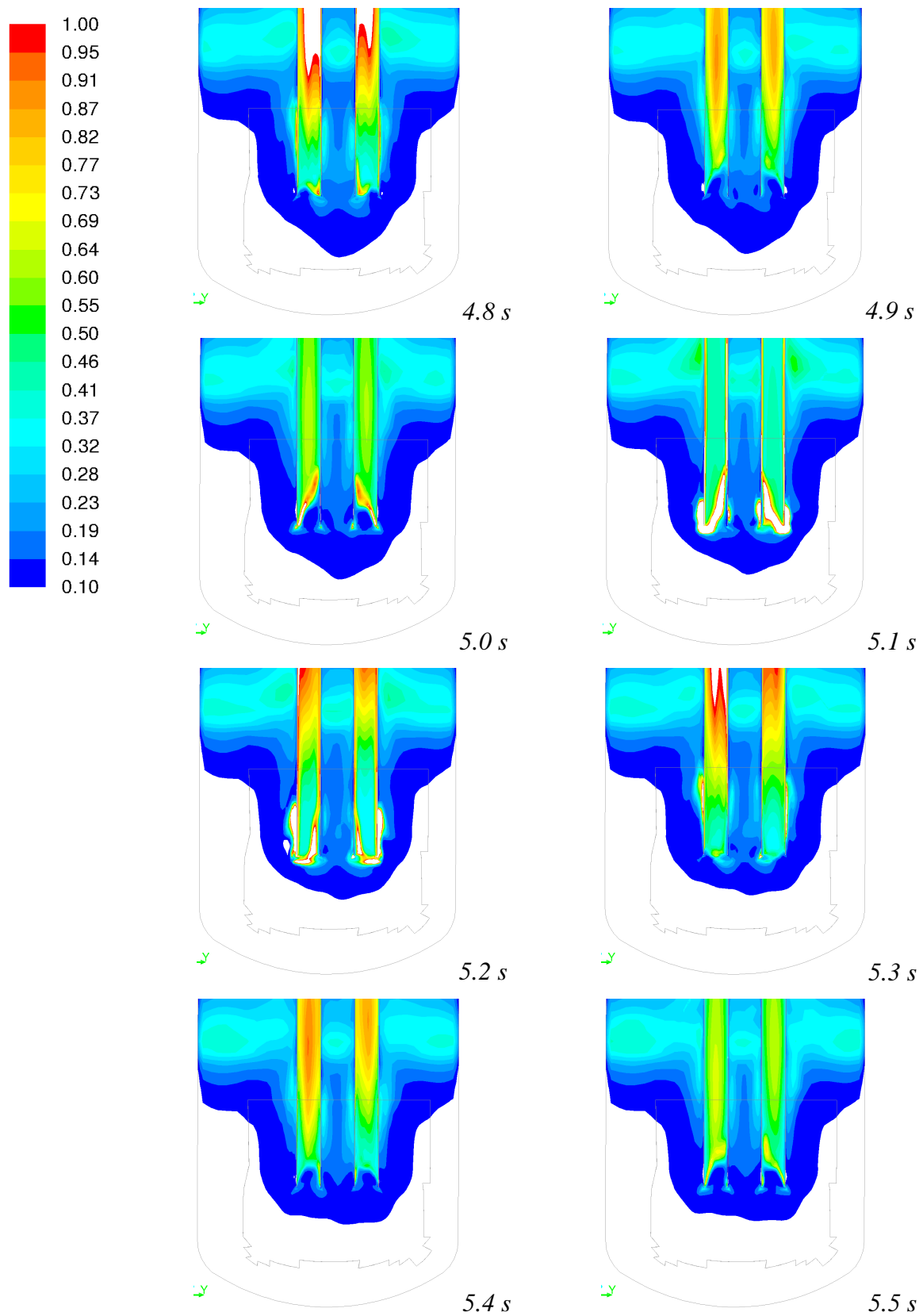


Figure 4. Heat transfer coefficient (MW/m<sup>2</sup>K) on the liquid side during the condensation of a vapor bubble. Note that the values below the scale and above the scale are not shown.



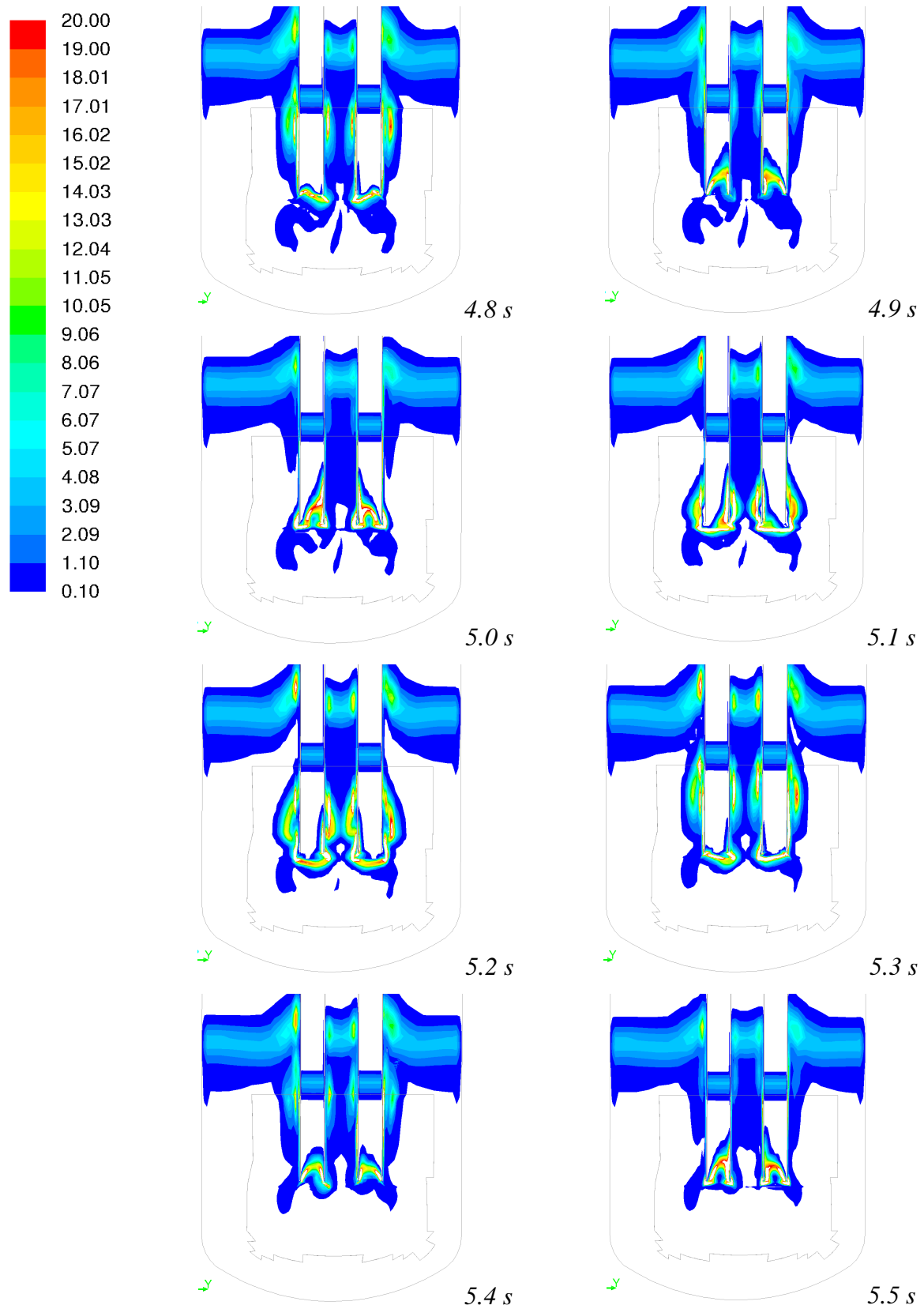


Figure 5. Interfacial area concentration (m<sup>-1</sup>) near the outlets of the vent pipes. Note that the values below the scale and above the scale are not shown.

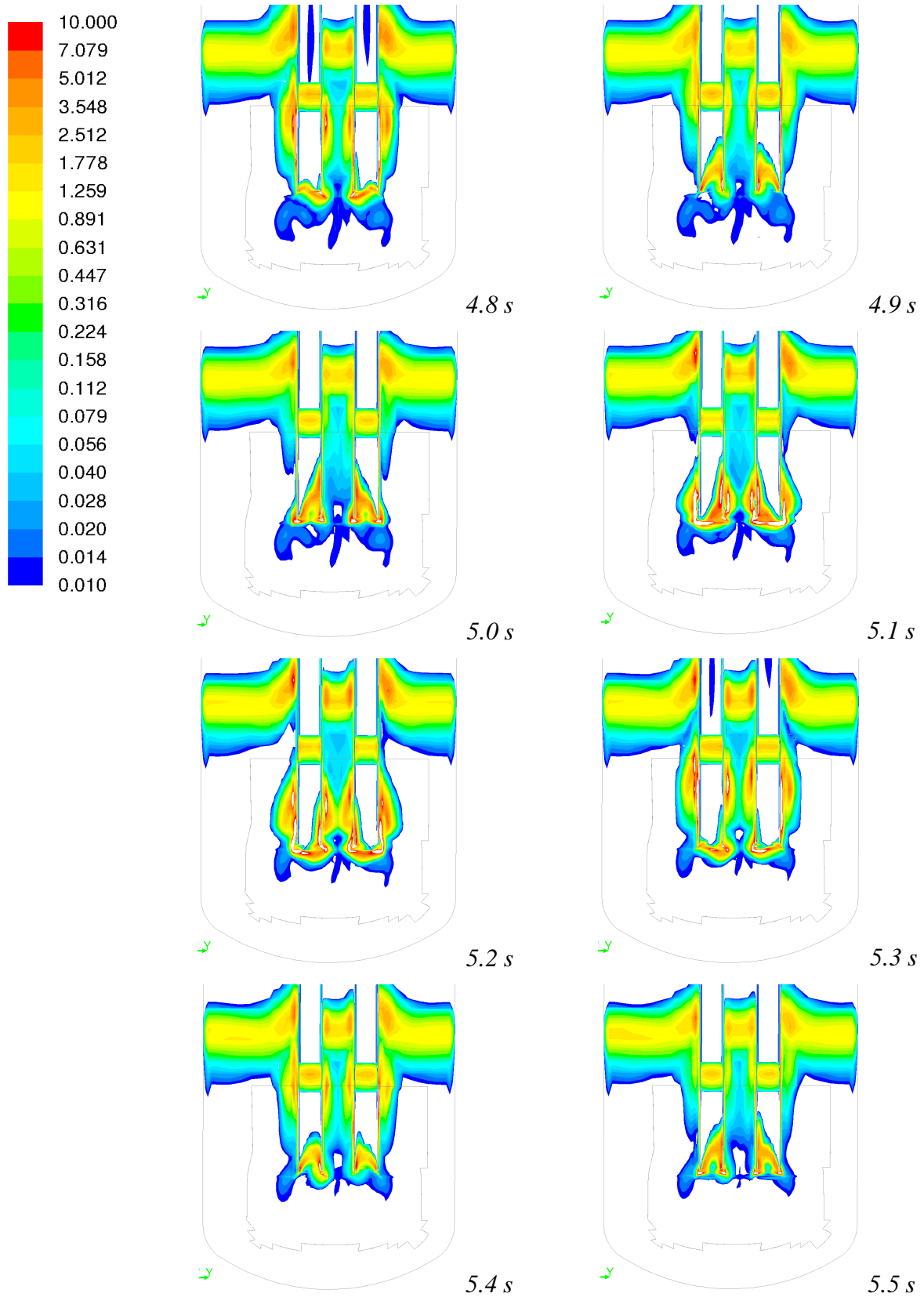


Figure 6. Volumetric heat transfer coefficient  $htc_{\text{water}} \times a_i$  (MW/m<sup>3</sup>K). Note that the scale is logarithmic. The values below the scale and above the scale are not shown.

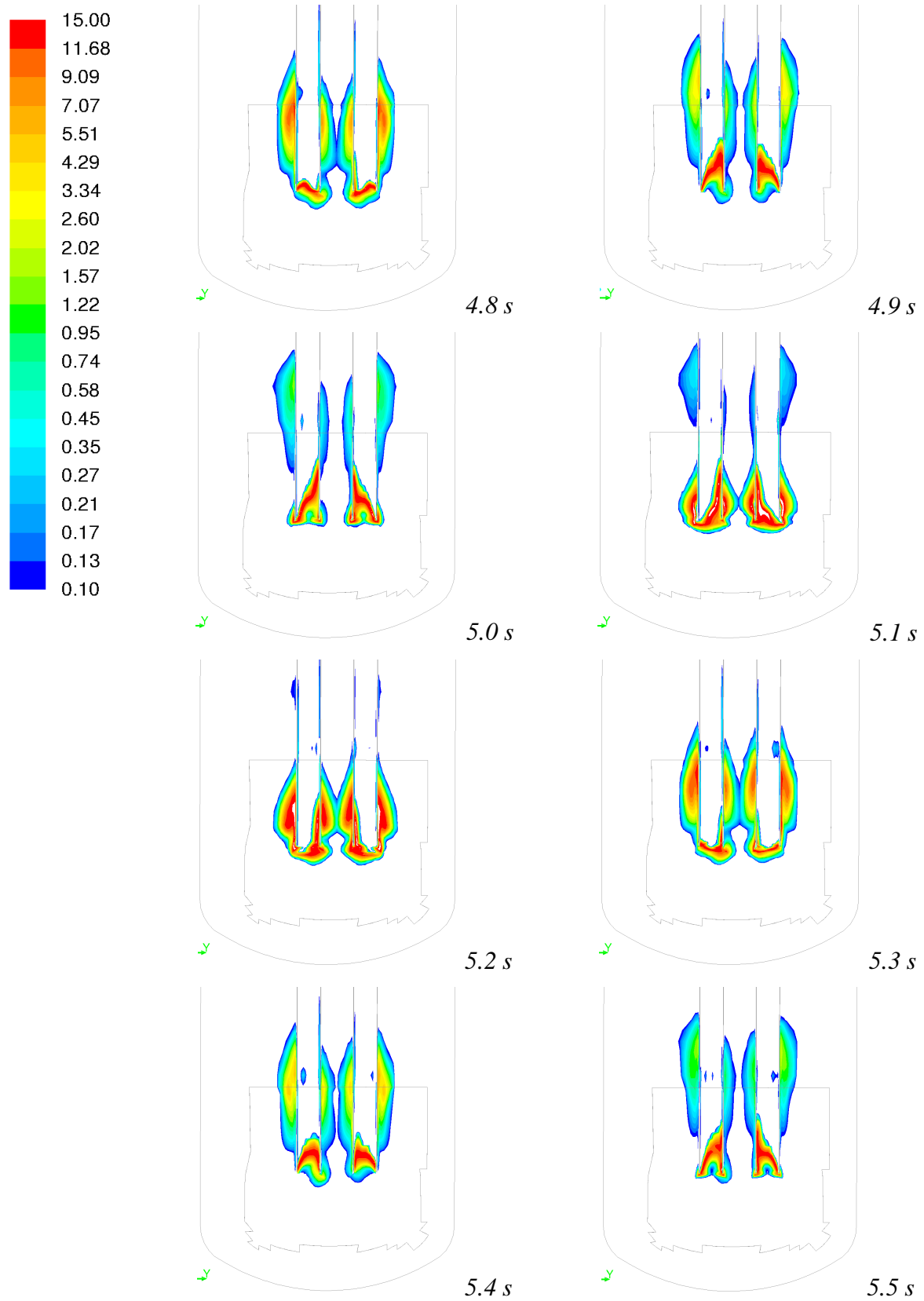


Figure 7. Mass transfer rate (kg/m<sup>3</sup>s) in direct contact condensation of a vapor bubble. Note that the scale is logarithmic. Values below the indicated scale are not shown.

### 3 Pressure loads due to collapsing vapor bubble

Eulerian FEM calculations were performed for the PPOOLEX experiment COL-01 by using the Abaqus 6.11 code. This experiment was chosen based on the fairly large pressure loads and structural displacements due to the rapidly condensing steam bubbles.

#### 3.1 Analysis of experiment COL-01

Four bubble collapses giving the largest pressure loads were searched from the experimental data. Sensor locations and a schematic picture of a toroidal bubble at the vent pipe outlet are shown in Figure 8 and Figure 9. From the high-speed video recordings, the maximum sizes of the toroidal bubbles right before the collapses were determined as is shown in Table 1 and in Figure 10. The collapse of the first bubble is shown in Figure 11. It is seen that the bubble sizes are fairly small in this experiment compared to some other experiments, but the pressure loads are nonetheless quite large. The small bubble sizes and large pressure loads indicate a large condensation rate of steam in the bubble.

Time signals of pressures as well as pool bottom displacement and acceleration are shown for the four bubble collapses in Figure 12 to Figure 17. From pressure P5, which is taken close to the vent pipe outlet, the characteristic pressure signal of a rapid steam bubble collapse can be seen: the first phase consists of an under-pressure phase during which water is sucked towards the center of the bubble, whereas the second phase consists of a rapid over-pressure peak as the volumetric water flow is rapidly decelerated. This characteristic behavior has been noted also by others, see e.g. Giencke (1981), McCauley et al. (1981) and Kukita and Namatame (1985). From the duration of the under-pressure phase shown well in pressure P5, the collapse times of the four bubbles can be estimated to be about 10 ms. This collapse time agrees approximately with the high-speed video recordings; the recording speed is 300 fps, which means that the collapses take place during about 3 frames. From pressure P5 it is also seen that the duration of the over-pressure peak is about 1...1.5 ms. From the video recordings it can be seen that the collapses do not usually occur fully axisymmetrically, i.e. duration of the collapses is usually not fully synchronous around the circumference of the vent pipe.

*Table 1. Maximum sizes and collapse times of four bubbles giving the largest pressure loads in PPOOLEX experiment COL-01.*

Bubble	Time	$r_{\max}$	$r_{\max, \text{average}}$	$R$	Collapse time
1	65.56 s	46 mm	47 mm	110 mm	~10 ms
2	99.35 s	37 mm			
3	100.74 s	55 mm			
4	137.04 s	50 mm			

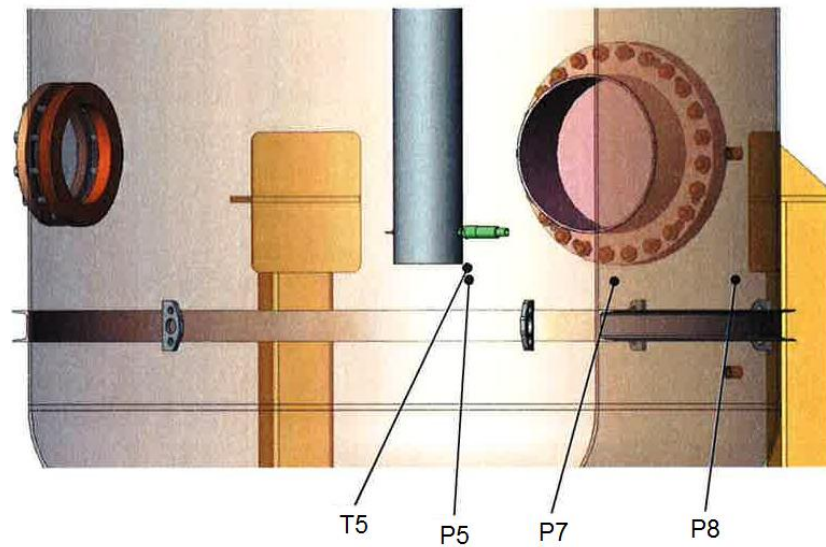


Figure 8. Sensor locations in the PPOOLEX experiment COL-01. (Laine et al., 2009)

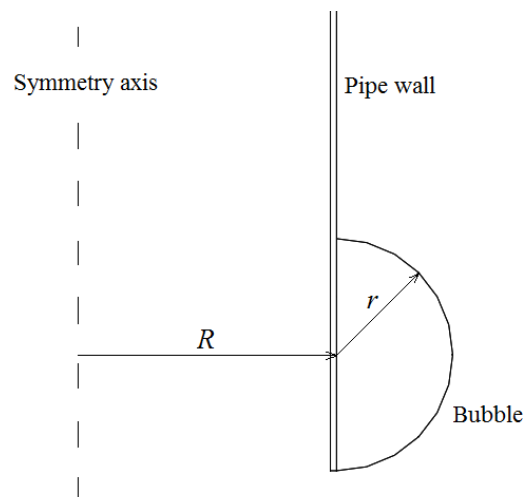


Figure 9. Schematic picture of a toroidal bubble at the vent pipe outlet.



Bubble 1



Bubble 2



Bubble 3



Bubble 4

*Figure 10. Four bubbles giving the largest pressure loads in PPOOLEX experiment COL-01. The bubbles are shown right before the collapse, i.e. when the bubble size is largest.*



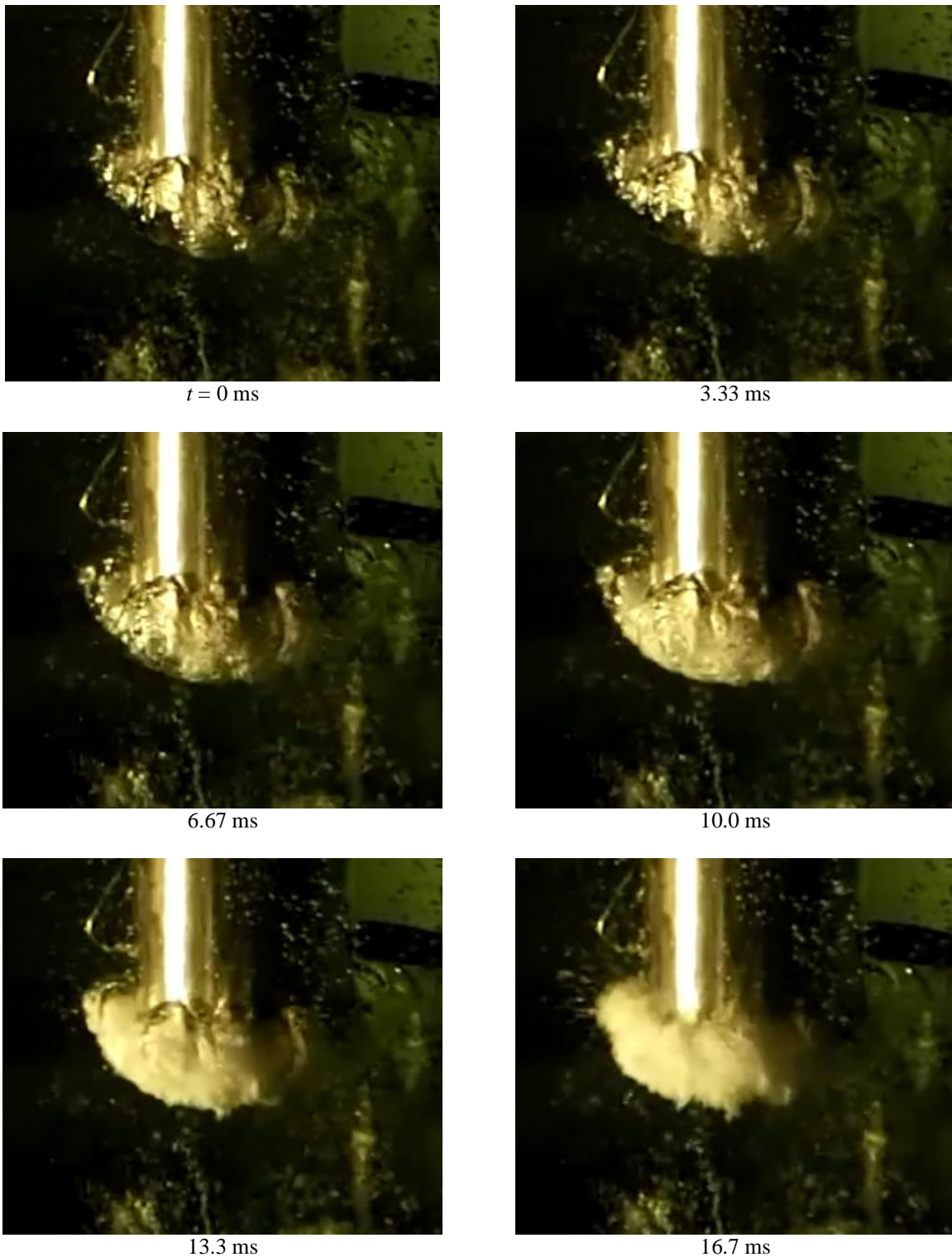
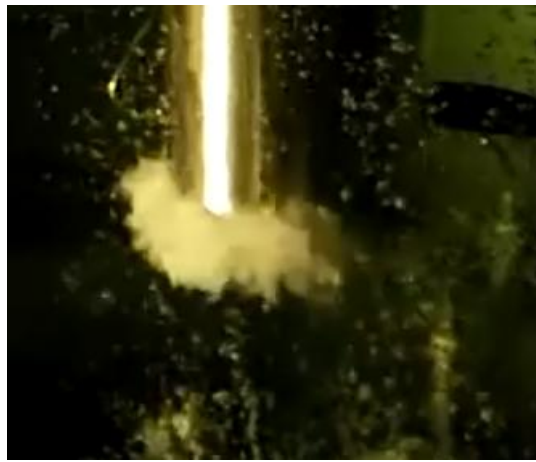
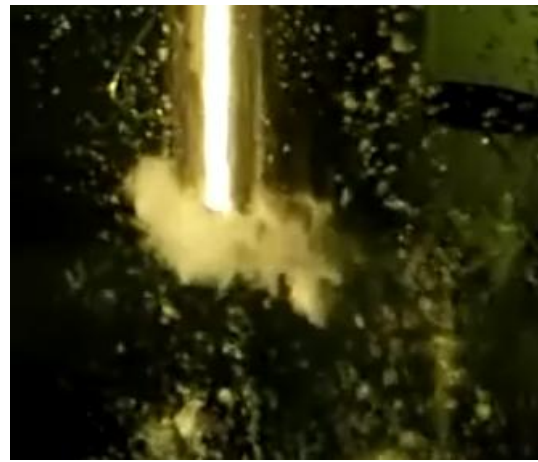


Figure 11. Collapse of Bubble 1 in PPOOLEX experiment COL-01 (continues on the next page).


 $t = 20.0 \text{ ms}$ 


23.3 ms



26.7 ms



30.0 ms



33.3 ms



36.7 ms

*Figure 11. Continues from the previous page.*



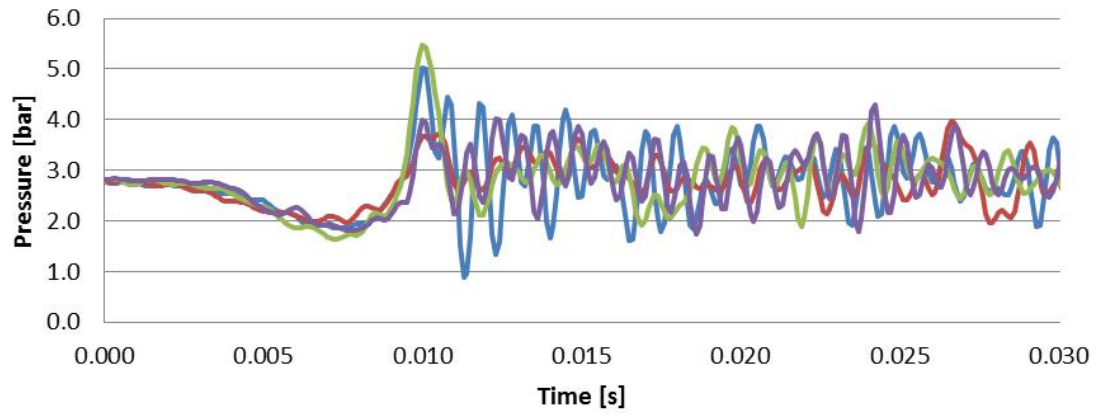


Figure 12. Pressure P5 measured in PPOOLEX experiment COL-01 (— Bubble 1, — Bubble 2, — Bubble 3, — Bubble 4).

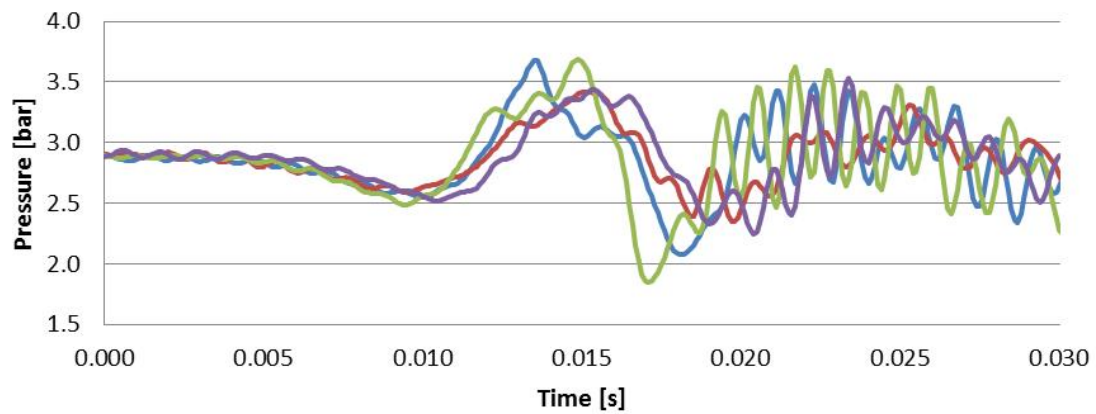


Figure 13. Pressure P6 measured in PPOOLEX experiment COL-01 (— Bubble 1, — Bubble 2, — Bubble 3, — Bubble 4).

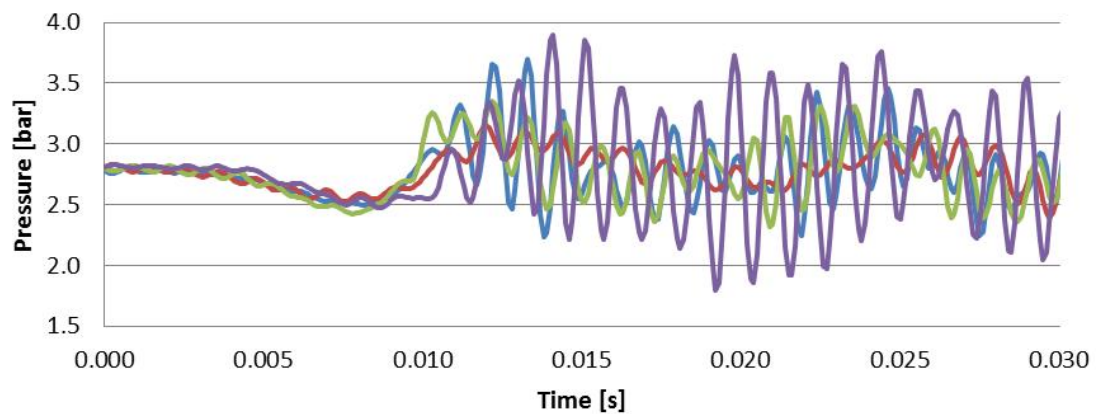


Figure 14. Pressure P7 measured in PPOOLEX experiment COL-01 (— Bubble 1, — Bubble 2, — Bubble 3, — Bubble 4).

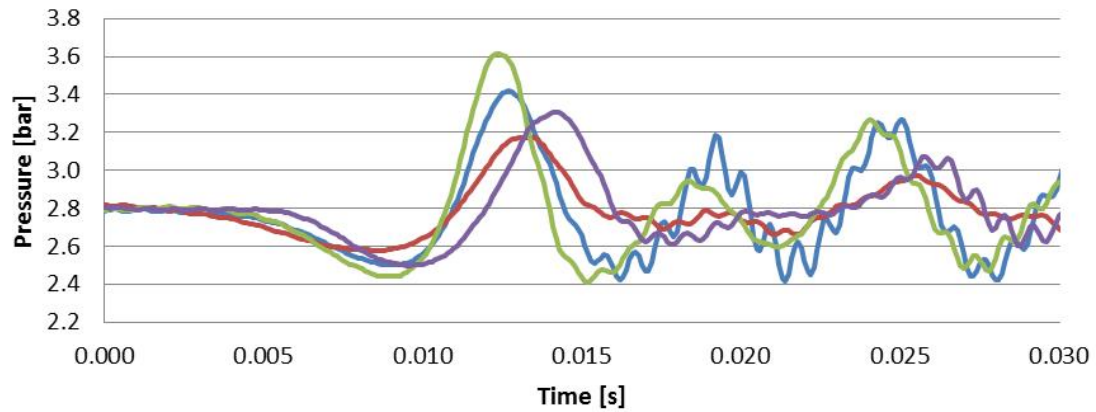


Figure 15. Pressure P8 measured in PPOOLEX experiment COL-01 (— Bubble 1, — Bubble 2, — Bubble 3, — Bubble 4).

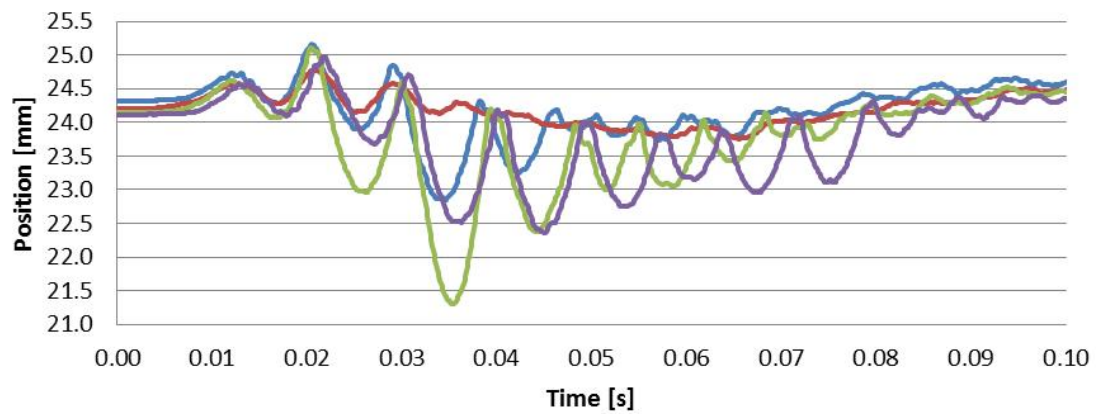


Figure 16. Pool bottom position measured in PPOOLEX experiment COL-01 (— Bubble 1, — Bubble 2, — Bubble 3, — Bubble 4).

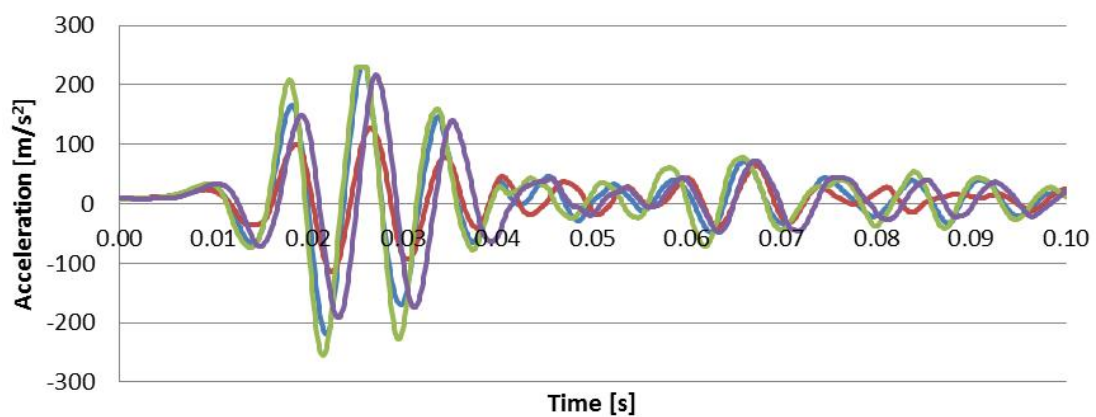


Figure 17. Pool bottom acceleration measured in PPOOLEX experiment COL-01 (— Bubble 1, — Bubble 2, — Bubble 3, — Bubble 4).

## 3.2 Eulerian FEM calculations

The new Eulerian method of Abaqus 6.11 was used for analyzing the rapid bubble collapses in simplified cases. In the Eulerian method, the numerical mesh is fixed in space and the material under consideration flows through the mesh, as in the CFD calculations. This is in contrast to the Lagrangian description used traditionally in structural analyses, where the numerical mesh moves and deforms with the material. The Eulerian description is well suited for situations involving extreme material deformations, such as those occurring in fluid flow, since the problems with mesh distortion can be avoided. However, additional considerations are needed in the Eulerian method to compute the motion of material boundaries, and the resulting description of the material boundaries is usually less accurate than in the Lagrangian method.

In Abaqus, the tracking of the material boundaries is based on the Volume-Of-Fluid (VOF) method, which is commonly used in CFD calculations of free-surface or multi-material flows. In the method, the material is tracked as it flows through the mesh by computing the volume fraction of the material in each element. The Eulerian material can also interact with the Lagrangian structural elements, resulting in a coupled Eulerian-Lagrangian (CEL) analysis; this analysis method can be used for modeling FSI.

In this work, we perform calculations of the bubble collapses by using one-dimensional spherically symmetric models and two-dimensional axisymmetric models. The ideal gas law is employed for the non-condensable gas in the bubble and a linear equation of state is used for water. The Eulerian method uses explicit time integration and hence time step needs to be quite short in the simulations. The calculations are computationally quite expensive and hence no three-dimensional models were used at this stage.

In the experiments by Puustinen (2006), even small amounts of air among the steam have suppressed the waterhammer loads due to the condensing bubbles. With mass fractions of about 1 %, the loads were still visible but the non-condensable gas had an effect on them. At mass fractions of 3 %, the damping of the waterhammer loads was practically complete. Therefore, interest in this work is in situations where the mass fraction of air is in the range of 0 ... 3 %. Assuming a total pressure of 1 bar, this corresponds to partial pressures of air of about 0 ... 1900 Pa.

### 3.2.1 Comparison of 1D and 2D models

We first compare pressure loads obtained for a collapse of spherical bubble in infinite fluid by using one- and two-dimensional models. In addition, results obtained by using the conventional Lagrangian stress-displacement elements and a one-dimensional model, as in the earlier calculations of Pättikangas et al. (2011), are included for comparison. In the earlier calculations, the Lagrangian method was validated against analytical solutions for situations where water may be assumed incompressible.

The initial radius of the bubble was set to 83 mm, which has the same volume as a toroidal bubble with dimensions  $R = 110$  mm and  $r = 47$  mm (see Figure 9). This bubble size is based on the average size of the four experimentally observed

bubbles. Meshes of the Eulerian models are shown in Figure 18. Element size in the bubble is about 2 mm for the coarse 1D mesh and for the 2D mesh. For the fine 1D mesh, element size is 0.1 mm at the bubble center and 1 mm at the bubble outer edge. Initial pressure in water was set to 1 bar and for air in the bubble to 500 Pa or 2000 Pa. Initial temperature was set to 20 °C. This corresponds to a situation where a small amount of non-condensable gas has been left in the bubble.

Pressure signals 200 mm from the bubble center are presented in Figure 19 and Figure 20. All models yield approximately the same results for the first phase of the collapse, but large differences exist in the peak amplitude for the case with lower initial pressure. The differences between the models diminish when the initial pressure is increased, i.e. when the non-condensable gas limits more the increase of water velocity in the final phase. The meshes need to be quite fine with a low initial pressure, since then the bubble size at the end of the collapse becomes small and the pressure pulse becomes sharp. The one- and two-dimensional Eulerian calculations yield approximately similar results with similar mesh densities. The hump in the Lagrangian calculation results from the bubble surface “bouncing” back after the collapse (see Pättikangas et al., 2011); although the Eulerian calculations behave similarly the hump is for some reason not shown.

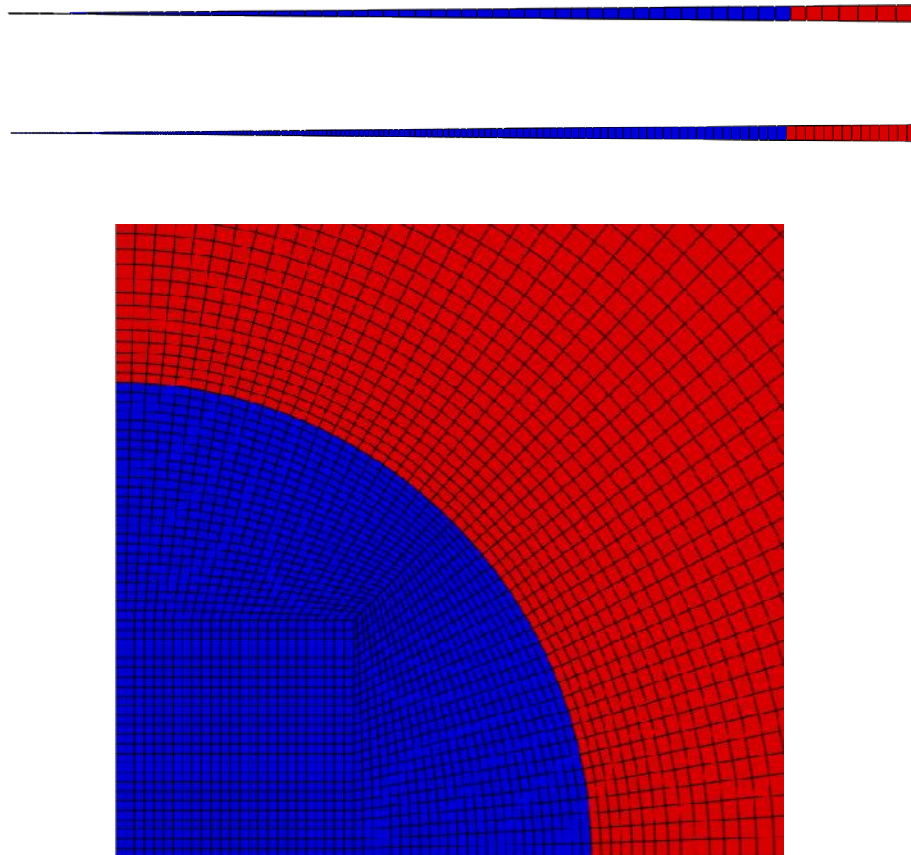


*Figure 18. One- and two-dimensional Eulerian FEM meshes of a spherical bubble. Initial volume fractions of air and water are shown with blue and red, respectively.*

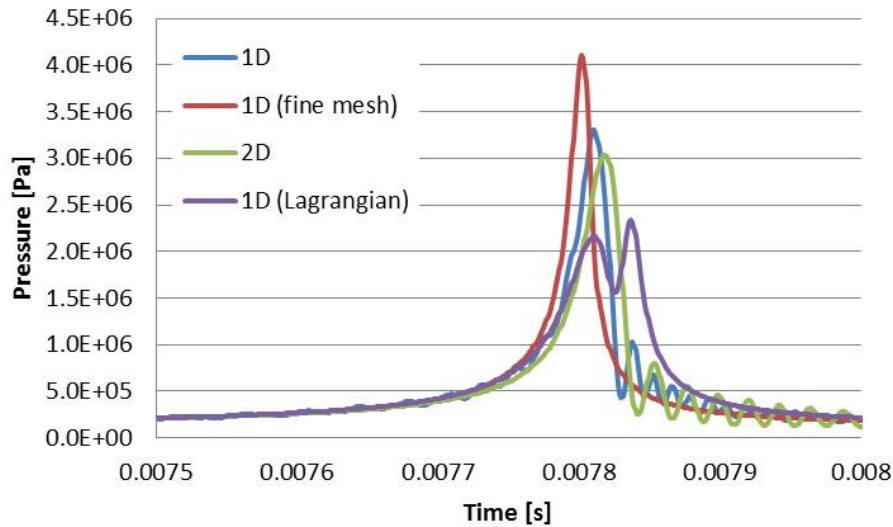


Figure 19. Pressure 200 mm from the bubble center for a spherical bubble. The bubble initial pressure is 500 Pa.

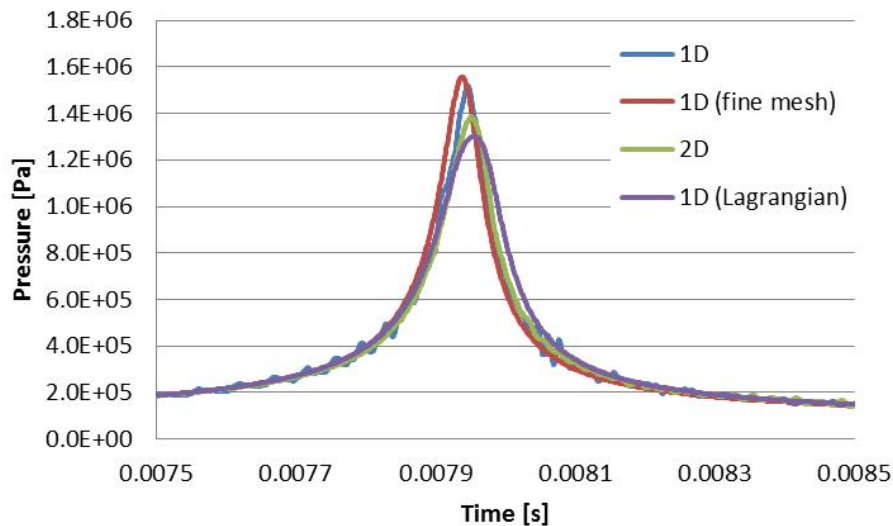


Figure 20. Pressure 200 mm from the bubble center for a spherical bubble. The bubble initial pressure is 2000 Pa.

### 3.2.2 Comparison of spherical and toroidal bubbles

In the following, comparisons are made for the collapse times and pressure loads resulting from the collapses of spherical and toroidal bubbles in infinite fluid. The two-dimensional Eulerian mesh with a toroidal bubble at the vent pipe outlet is shown in Figure 21. Here the same initialization is used in the bubble and in the vent pipe.

The collapse of a spherical bubble in infinite incompressible fluid and having constant pressure difference can be solved analytically (see e.g. Pättikangas et al., 2011). The collapse time is



$$t_{\text{tot}} = 0.9147 R_0 \left( \frac{\rho}{\Delta p_B} \right)^{1/2}$$

where  $R_0$  is the initial bubble radius,  $\rho$  is the fluid density and  $\Delta p_B$  is the pressure difference. The pressure difference is  $\Delta p_B = p_\infty - p_B$ , where  $p_\infty$  is pressure far away from the bubble and  $p_B$  is pressure in the bubble. Earlier calculations (Pättikangas et al., 2011) have shown that the collapse time is practically unaffected by the water compressibility, although the compressibility has a large effect on the resulting pressure load. This is because the water velocity grows large only at the late phase of the collapse. Therefore, we compare the collapse times of the toroidal bubble against the analytical solution of the spherical bubble.

In Figure 22, the collapse time is plotted as a function of the pressure difference. For the toroidal bubble, values  $R = 110$  mm and  $r = 47$  mm were used based on the four experimental bubbles. The radius of the spherical bubble was set accordingly to  $R = 83$  mm, i.e. so that the both bubbles have equal volumes. It is seen that the collapse times are approximately equal for the both bubbles in spite of their differing shapes.

In Figure 23, the collapse time is plotted as a function of effective bubble radius. Here the effective radius is defined as the radius of an equivalent spherical bubble having the same volume as the toroidal bubble in question. The different sized toroidal bubbles were obtained by linearly scaling the FEM model, as is shown in Table 2. The pressure difference was set to  $\Delta p_B = 1$  bar. It is seen that also in this case, the collapse times of the bubbles are quite similar. The collapse time depends linearly on the (effective) bubble radius also for the toroidal bubble.

The effect of bubble initial pressure on the pressure pulse is studied in Figure 24 to Figure 26 by using initial pressure of 1 bar in the water. Note that in Figure 24, pressure is presented at the sensor P5 for the torus and for the sphere 200 mm from the bubble center, where the pressure amplitude is about the same as for the torus. It is seen that the pressure load depends similarly on the bubble initial pressure in both cases. Further away from the bubble, the both cases yield about the same pressure load when the initial pressure is above 5000 Pa. With lower initial pressures, the pressure pulse gets too sharp for the meshes away from the bubble and numerical diffusion affects the results considerably. Based on Figure 24, the pressure load 1 m from the bubble would be about the same also with lower initial pressures for the sphere and for the torus. The pulse width was determined approximately from the pressure signals and is about the same for both cases with different initial pressures.

The effect of sound velocity in water on the pressure pulse is studied in Figure 27 and Figure 28 by using initial pressure of 1 bar in the water and void initialization in the bubble. Here pressure is presented at the sensor P5 for the torus and 200 mm from the bubble center for the sphere. It is seen that the pressure amplitude depends linearly on the sound velocity in both cases. The pulse width grows for the both cases as the sound velocity is decreased and becomes clearly longer for the sphere when the sound velocity is low.

In Figure 29 and Figure 30, the pressure pulse amplitude and width are plotted as functions of the effective bubble radius. Here initial pressures 1 bar and 2000 Pa

were used in the water and in the bubble, respectively. Four different sizes were calculated as shown in Table 2. For the torus, pressure is presented at a location corresponding to the sensor P5, but note that also this location is scaled along the system dimensions. For the sphere, pressure is presented accordingly 100, 200, 400 and 800 mm from the bubble center. Firstly, the pressure amplitude is constant which means that the peak volume acceleration grows linearly as the system scale is increased; this is consistent with the earlier one-dimensional calculations by Pättikangas et al. (2011). Secondly, as for the collapse time, also the pulse width depends linearly on the system scale.

Table 2. Dimensions of four toroidal bubbles.  $R$  and  $r$  represent the vent pipe radius and tube radius of the torus, as shown in Figure 9.

$R$ [mm]	$r$ [mm]	$R_{\text{eff}}$ [mm]
55	23.5	41
110	47	83
220	94	166
440	188	332

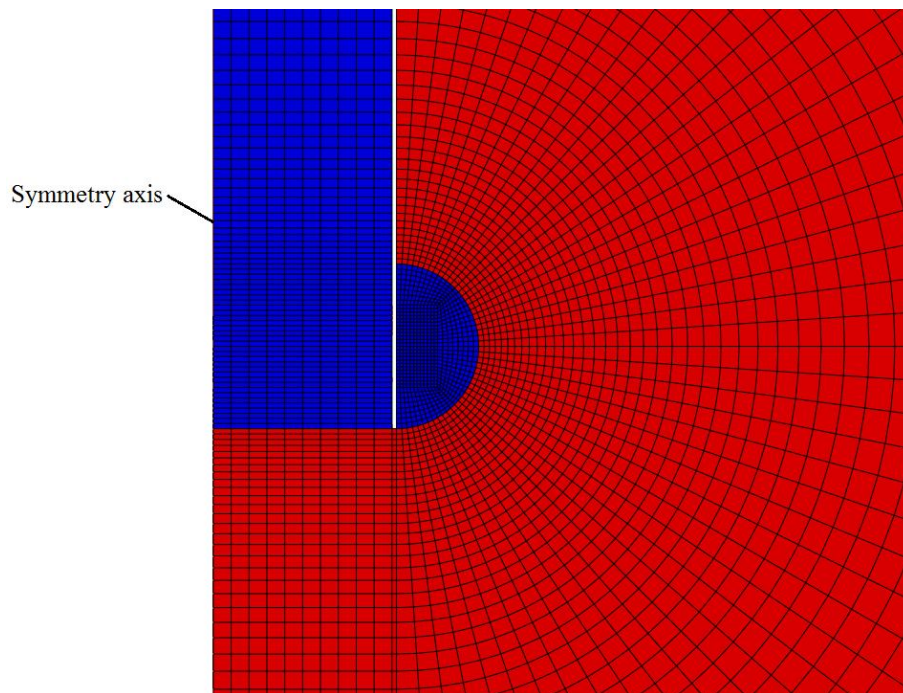


Figure 21. Axisymmetric mesh with a toroidal bubble at the vent pipe outlet.

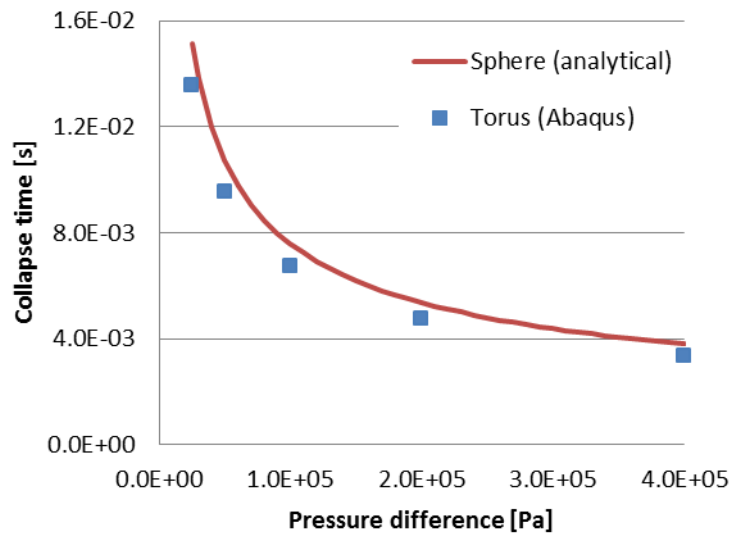


Figure 22. Bubble collapse time as a function of pressure difference.

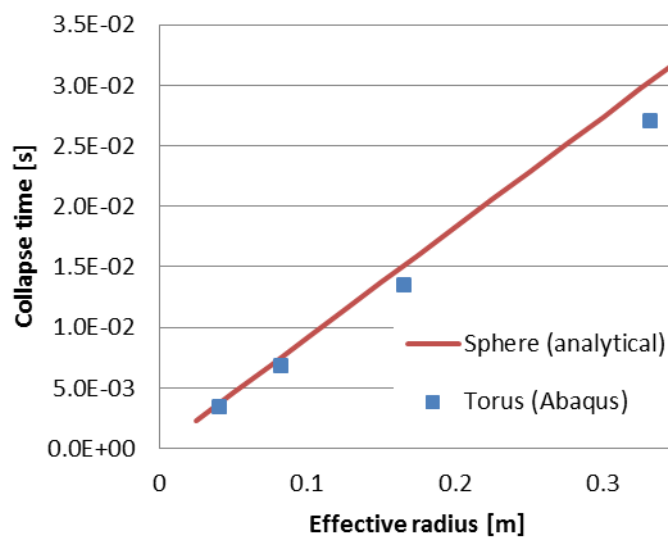


Figure 23. Bubble collapse time as a function of effective radius.



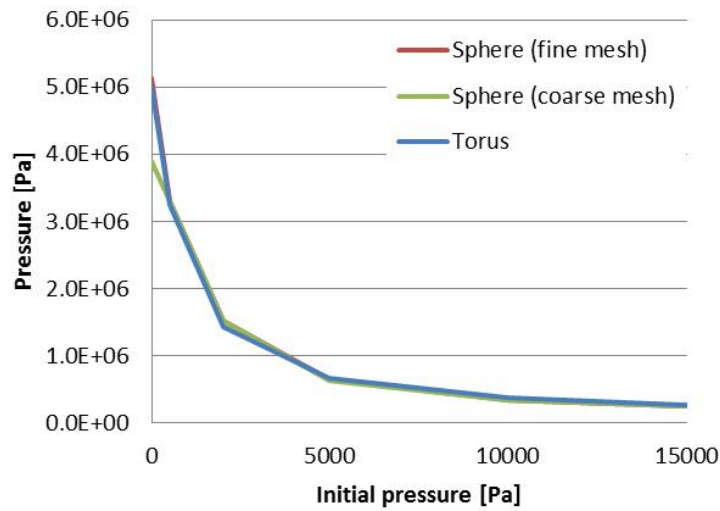


Figure 24. Effect of bubble initial pressure on pressure amplitude at sensor P5 (torus) and 200 mm from bubble center (sphere).

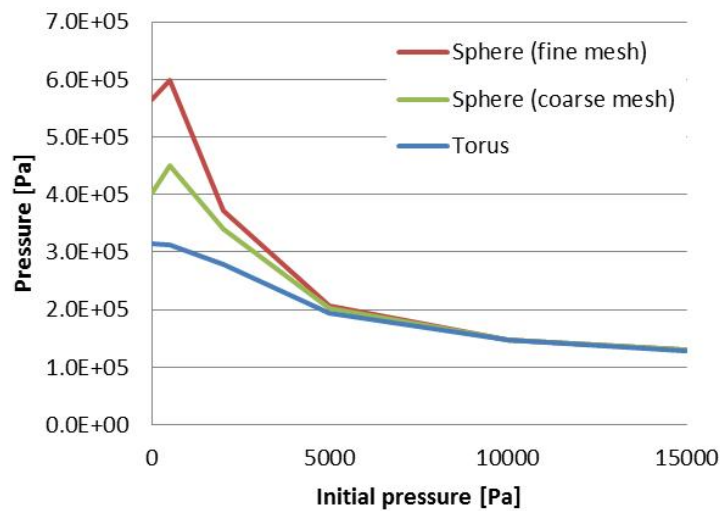


Figure 25. Effect of bubble initial pressure on pressure amplitude 1 m from bubble.

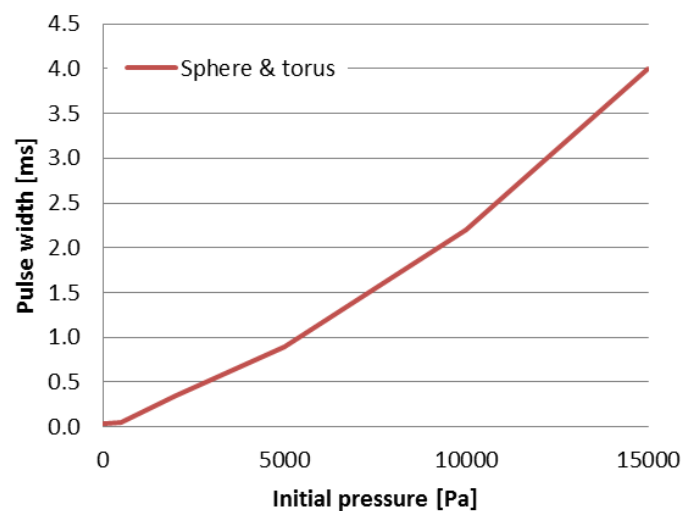


Figure 26. Effect of bubble initial pressure on pressure pulse width.

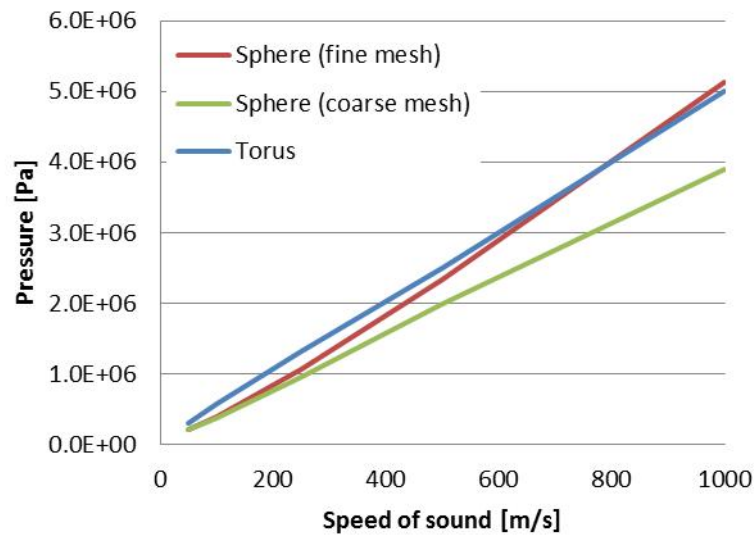


Figure 27. Effect of sound velocity in water on pressure amplitude at sensor P5 (torus) and 200 mm from bubble centre (sphere).

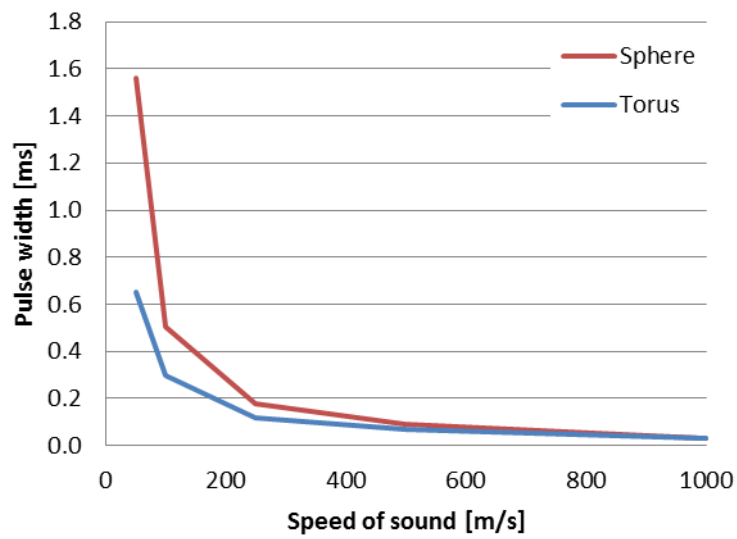


Figure 28. Effect of sound velocity in water on pressure pulse width.

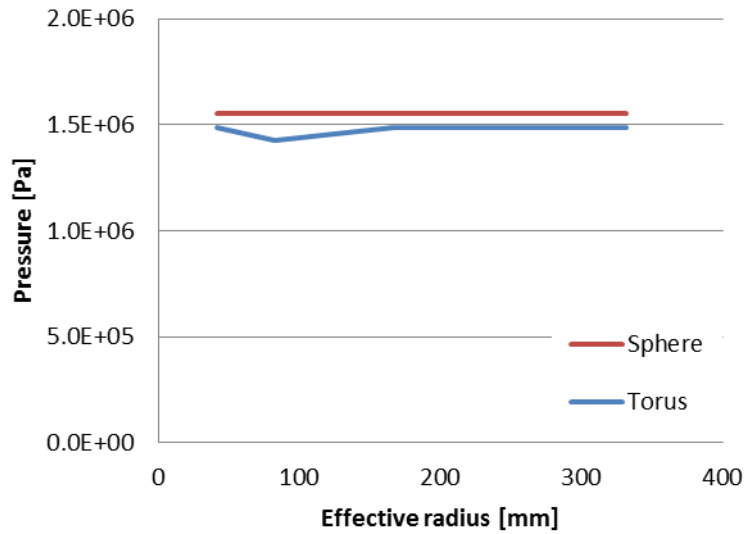


Figure 29. Pressure amplitude as a function of effective radius. Note that the monitoring location is scaled along the system dimensions.

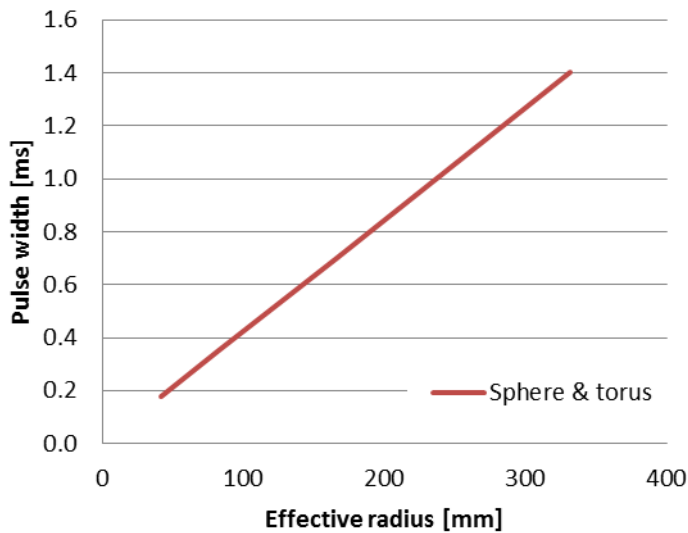


Figure 30. Pressure pulse width as a function of effective radius.

### 3.2.3 Modeling of the PPOOLEX facility

The axisymmetric Eulerian model of the PPOOLEX facility is shown in Figure 31. The dimensions of the model correspond to the real pool, but the vent pipe has been here assumed at the center of the pool due to the axisymmetry. The drywell and wetwell gas spaces are separate as in the experiments. Here we initialize for simplicity void for the gas in the bubble, in the vent pipe and in the drywell. Same constant pressure is initialized in the water and in the wetwell gas space. The initial size of the bubble at the vent pipe outlet was chosen based on the average value of the four experimentally observed bubbles. Referring to Figure 9, the initial dimensions of the bubble are  $R = 110$  mm and  $r = 47$  mm.

Figure 32 shows calculated pressures at the sensor P5 for three different initial pressures in the wetwell: 0.25 bar, 0.5 bar and 1 bar. These pressures are also the pressure differences causing the collapse, since the bubble has been assumed to consist of void. Firstly, it is seen that the collapse times are about 15 ms, 11 ms and 7.6 ms, which are quite close to the experimental value of about 10 ms. Secondly, the pressure peaks are considerably higher and sharper than in the experiments. The duration of the pressure peaks is only about 0.05 ms, compared to the experimental value of about 1 ms. The amplitude of the pressure peaks is about an order of magnitude too high. Comparison of the calculated and experimental collapse times indicates that the pressure difference used in the calculations is approximately correct.

The experiments indicate that the pressure difference causing the collapse grows gradually, as shown in the under-pressure phase of pressure P5 in Figure 12. This is due to the finite condensation rate of steam in the bubble. Giencke (1981) notes that a linearly varying pressure difference has been observed experimentally and uses linear and quadratic pressure differences in analytical calculations of the bubble collapse. Below we make calculations with the PPOOLEX model by using linear and quadratic pressure differences:

$$\Delta p_B = C_l t \quad \Delta p_B = C_q t^2$$

where  $C_l$  and  $C_q$  are constants which determine the rate of the pressure difference growth. Here the pressure difference is  $\Delta p_B = p_0 - p_B$ , where  $p_0$  is pressure in the wetwell gas space and  $p_B$  is pressure in the bubble. The pressure in the wetwell gas space is taken here as constant. The constants  $C_l$  and  $C_q$  are iterated manually so that the experimentally observed collapse time results.

Calculated pressure signals at the sensor P5 are shown in Figure 33 and Figure 34 for the linear and quadratic cases with two different values of the constants. The calculated pressures are compared with the experimental ones in Figure 35 for the cases where the constants have been iterated to give the correct collapse time. Here we consider only the under-pressure phase since the calculated over-pressure peaks tend to become much higher than in the experiments. Note that the calculated pressures have been offset so that the initial pressure level is the same as in the experiments, i.e. about 2.8 bars. This is the largest possible pressure difference in the experiments.

Overall, the linear pressure difference case is closer to the experimental data. For the quadratic case, the pressure difference becomes too high in the late phase of the collapse, although the shape of the pressure signal for the early phase is better represented than for the linear case. It should be noted that the sensor P5 lies close to the vent pipe outlet and the pressure amplitude is hence quite sensitive to the exact sensor location. Also, the initial bubble volume may be in the calculations somewhat larger than is on the average for the four experimental bubbles, since the bubble surface is quite rough in the experiments (see Figure 10).

There are several possible reasons for the low and wide experimental pressure peaks. Firstly, the bubble shapes are fairly irregular and there is usually some difference in the duration of the collapse around the circumference of the vent pipe. When the collapse occurs at slightly different instants of time around the

circumference, energy released in the collapse is spread along a wider time span. Secondly, the bubble may in reality break into a two-phase mixture, especially in the late phase of the collapse, which would soften the water-hammer. As shown in Figure 11, the bubble surface appears to be very irregular right at the time of the collapse. Thirdly, non-condensable gas left from the condensed steam may lower and broaden the pressure peaks, although the experiments (Puustinen, 2006) and present calculations indicate that the amount of non-condensable gas is too small to cause such a large difference. Fourthly, there may be a significant amount of steam left in the bubble in the important final phase, which could soften the water-hammer considerably. The results shown in Figure 35 indicate that absolute pressure inside the bubble is at minimum as high as about 1 bar, which in turn indicates that there is a significant amount of gas left in the bubble. The condensation rate may not be large enough in the final phase to condense out all of the steam before the moment of maximum volume acceleration, since in the final phase flow velocity near the bubble grows quite large and the bubble becomes small. The possible rise of steam pressure in the final phase could not be taken into account in the present calculations.

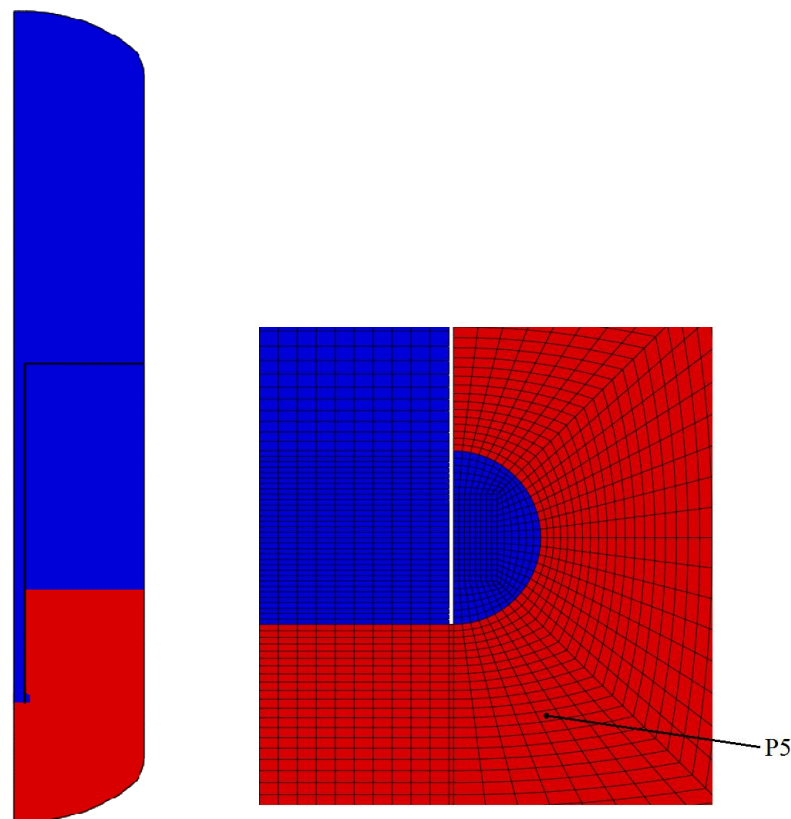


Figure 31. Axisymmetric Eulerian model of the PPOOLEX facility. Mesh near the vent pipe outlet and location of the P5 sensor is shown on the right.

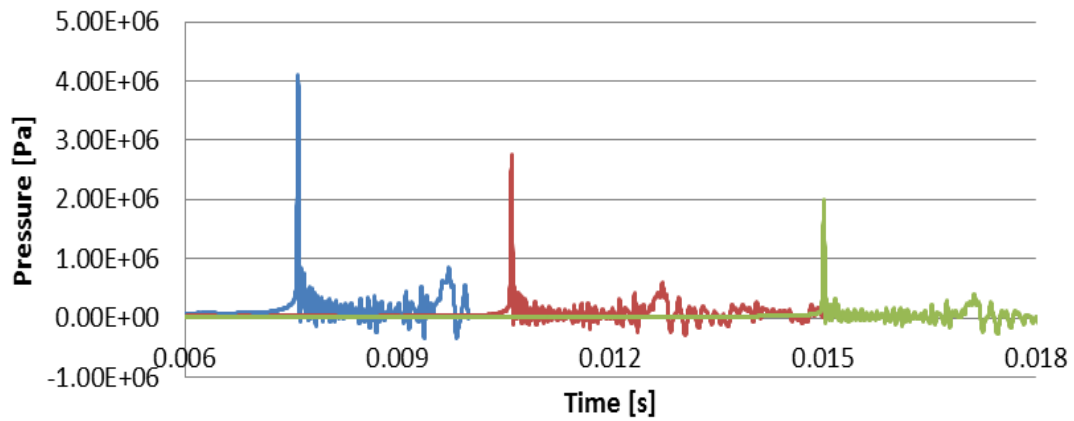


Figure 32. Pressure  $P_5$  calculated with different constant pressure differences ( $\Delta p_B = 1$  bar,  $\Delta p_B = 0.5$  bar,  $\Delta p_B = 0.25$  bar).

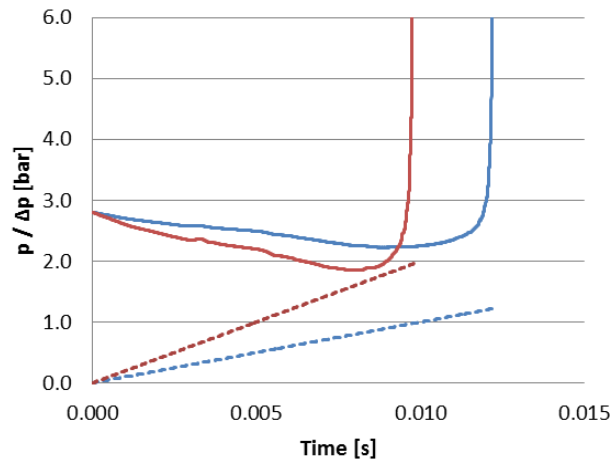


Figure 33. Pressure  $P_5$  calculated with linear pressure difference ( $P_5 C_l = 100$  bar/s,  $P_5 C_l = 200$  bar/s,  $\Delta p_B C_l = 100$  bar/s,  $\Delta p_B C_l = 200$  bar/s).

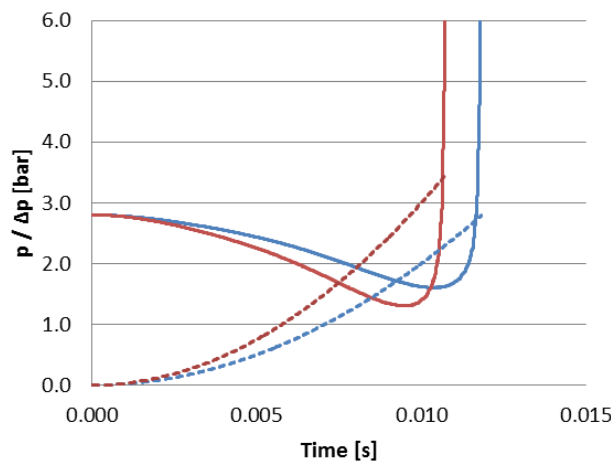


Figure 34. Pressure  $P_5$  calculated with quadratic pressure difference ( $P_5 C_q = 20000$  bar/s<sup>2</sup>,  $P_5 C_q = 30000$  bar/s<sup>2</sup>,  $\Delta p_B C_q = 20000$  bar/s<sup>2</sup>,  $\Delta p_B C_q = 30000$  bar/s<sup>2</sup>).

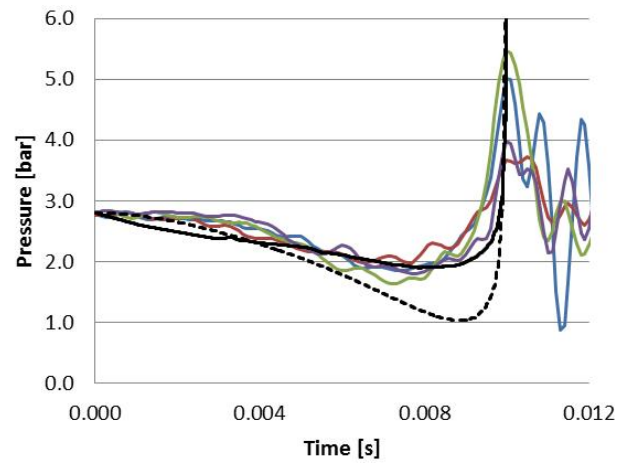


Figure 35. Measured and calculated pressure  $P_5$  in PPOOLEX experiment COL-01 (— Bubble 1, — Bubble 2, — Bubble 3, — Bubble 4, — linear  $C_l = 185 \text{ bar/s}$ , --- quadratic  $C_q = 40800 \text{ bar/s}^2$ ).

## 4 Analysis of the desynchronization of bubble collapses

### 4.1 Comparison between visual observations and measured pressures

The behavior of a pressure suppression containment of a BWR is studied with the help of experiments performed at the Lappeenranta University of Technology with the PPOOLEX facility. PPOOLEX is a scaled-down two-compartment model of a pressure suppression containment of a BWR. The focus of this study was the experiment PAR-10, in which steam is discharged through two parallel blowdown pipes into the condensation pool filled with sub-cooled water. The high speed video footage covers time span 500 - 530 s, during which chugging took place. The purpose was to compare the measured pressure data to the visually observed behavior. More detailed description of the experiment PAR-10 is presented by Puustinen et al. (2011).

The PPOOLEX test facility and the locations of the pressure gauges are presented in Figure 36. The pressure gauges P1 and P21 are placed at the same height inside the blowdown pipes, whereas pressure gauge P6 is located at the bottom of the pressure vessel. From this on, the pipes containing pressure gauge P1 and pressure gauge P21 are referred to as pipe 1 and pipe 2 respectively. The pressure-time history from pressure gauges P1, P21 and P6 are presented in Figure 37, Figure 38 and Figure 39 respectively. Every time an incident was observed in the video at the pipe outlet, the time was marked down and the event was described. All observed events are marked as red dots in the figures. When a large toroidal steam bubble formed at the pipe outlet, which rapidly condensed, the event was considered as clear chugging event. Those events are marked as white dots in the time-pressure histories. Pipe 1 is located at the background in the video image, which made the interpretation of events in the pipe1 slightly more difficult. This explains why some events taking place at the outlet of pipe 1 are not observed, whereas nearly all pressure fluctuations are observed as events at the outlet of pipe 2. The pressure gauge P6 is at the bottom of the pool, hence the measured pressure is affected largely also by the movement of the pool structure.



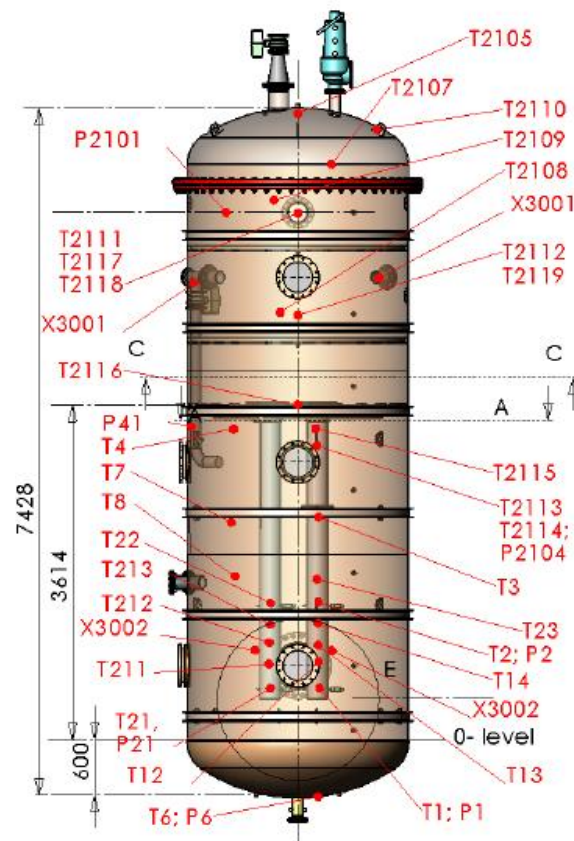


Figure 36. Location of measuring instruments (Puustinen et al., 2011).

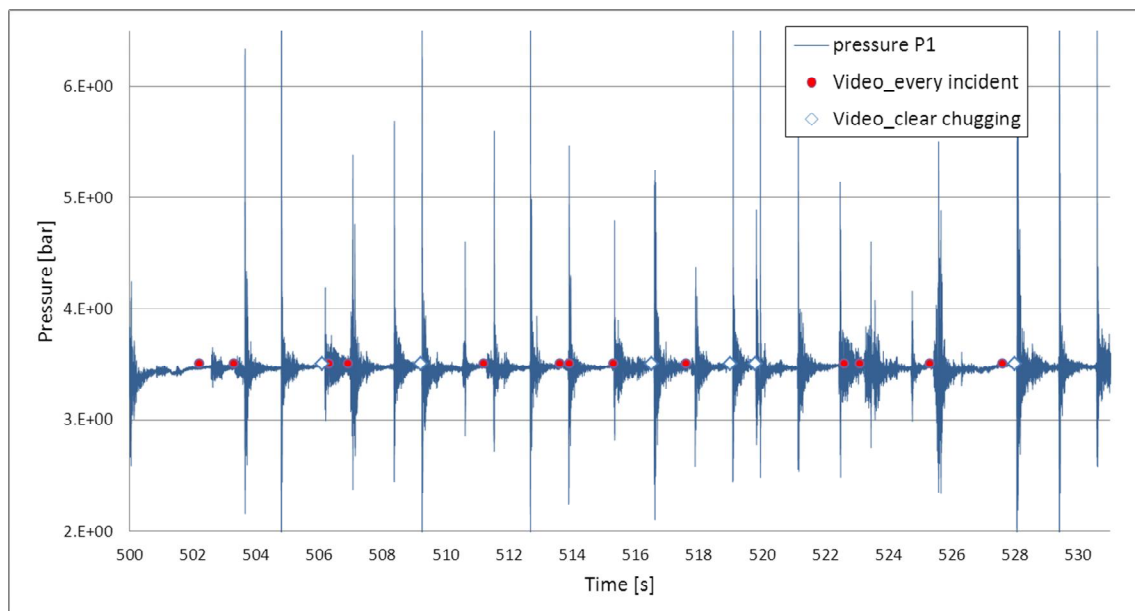


Figure 37. Time-pressure history from pressure gauge P1.

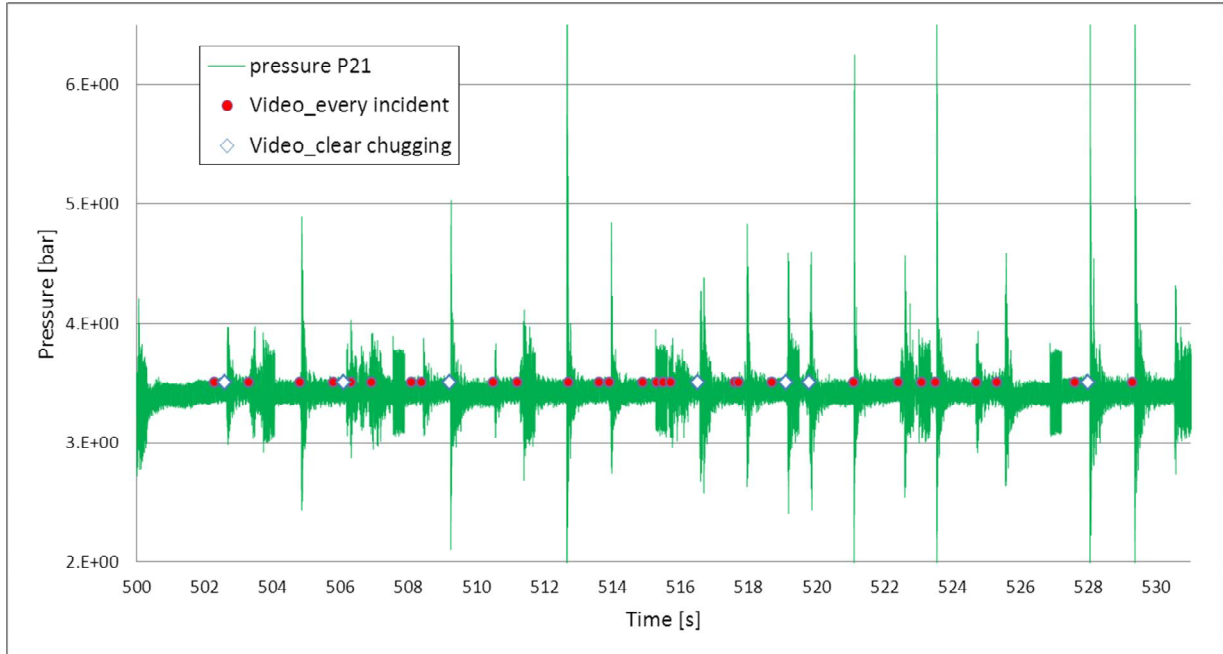


Figure 38. Time-pressure history from pressure gauge P21.

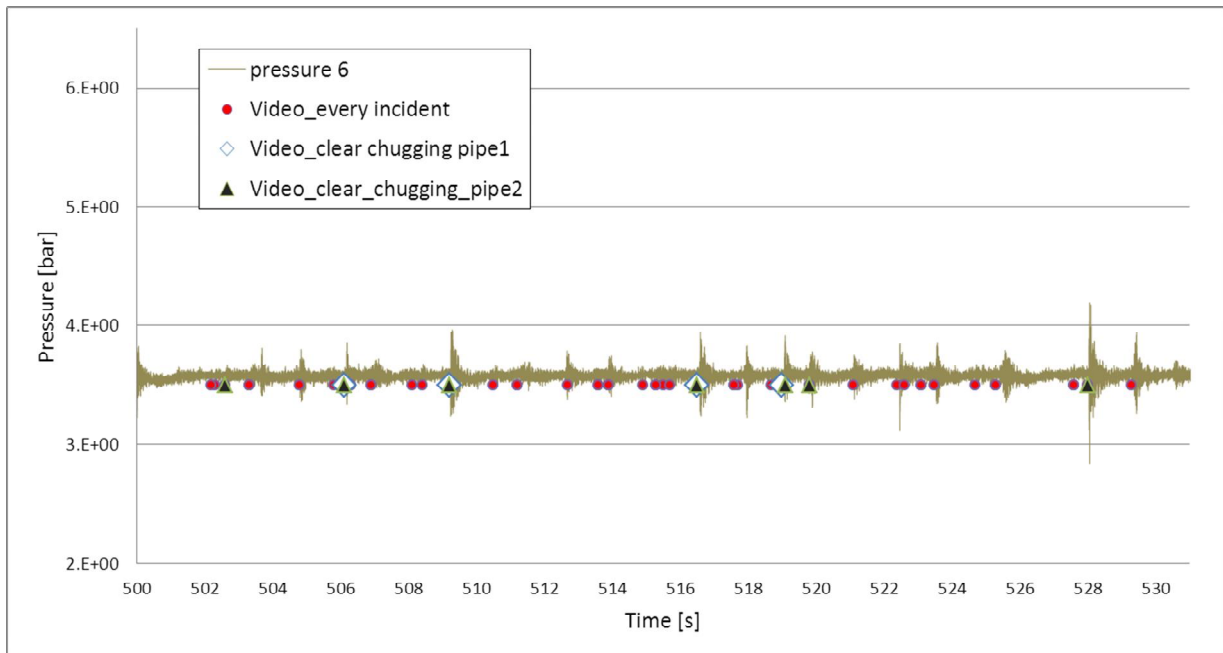


Figure 39. Time-pressure history from pressure gauge P6.

By looking at the figures, one may conclude, that the times of the observed events match quite well to the measured pressure fluctuations. The time of the incident in the video cannot be determined as accurately as the pressure fluctuation in the data, which might explain the small differences in time between observation and measured pressure peak. The following conclusions were made from the observations:

- High pressure peaks in pipe 1 or pipe 2 are not necessarily observed as clear chugging events and events marked as clear chugging events do not necessarily produce large pressure peaks.

- In the large scale, the events tend to occur at the same time in both pipes. Additionally, events that are considered clear chugging events occur simultaneously.
- Almost every time that chugging is observed, relatively intensive pressure fluctuation is measured at the pool bottom, but peaks may occur even if chugging is not observed.

Events that were observed, but not marked as clear chugging events comprise of events during which bubble was observed to penetrate from the pipe outlet, but either it did not condensate rapidly, but slowly withdrew back in to the pipe, or it occurred in the form of condensing of many small bubbles. Some events were observed only as blasts inside the pipe after which water advanced rapidly from the pipe, leaving the pipe to vibrate. This kind of events produced the largest pressure peaks, which can be explained by the fact that in this case the condensation has taken place in the pipe, causing the water that fills the void to flush in the direction of the pressure gauge.

## 4.2 Desynchronization of chugging between two vent pipes

The desynchronization of chugging between two pipes was studied by examining the measured pressures in pipe 1 and pipe 2. Chugging initiated approximately at time  $t = 500$  s and pressures were measured up till  $t = 955.4995$  s. The measuring frequency was 2000 Hz, i.e. pressure was measured between every 0.0005 seconds. Times of pressure peaks were carefully determined from both pipes. Chugging phase is distinguishable in most pressure peaks. It is characterized by pressure decrease, meaning that the bubble is collapsing and thus sucking water towards its center. This phase is followed by sudden increase in pressure, resulting from the rapid deceleration of the water volumetric flow. However the shape of some pressure fluctuations was such that the time of peak under pressure followed by peak pressure was not distinguishable and hence the desynchronization time between two pipes could not be determined. On the basis of visual examination of high-speed video footage and pressure measurement, the blurred events in the time-pressure events are due to the fact that the steam bubble actually consists of many toroidal shaped bubbles which do not condense simultaneously, but the chugging phase is divided into partial condensations of the bubble. In some rare cases, pressure fluctuation took place at one pipe while the pressure in the other pipe was relatively steady. Obviously in this case the desynchronization time was not determined. Example of this kind of case is presented in Figure 40 and an example of two distinguishable chugging events is presented in Figure 41. Only events where desynchronization time could be clearly determined were selected for the statistical examination of the variation.

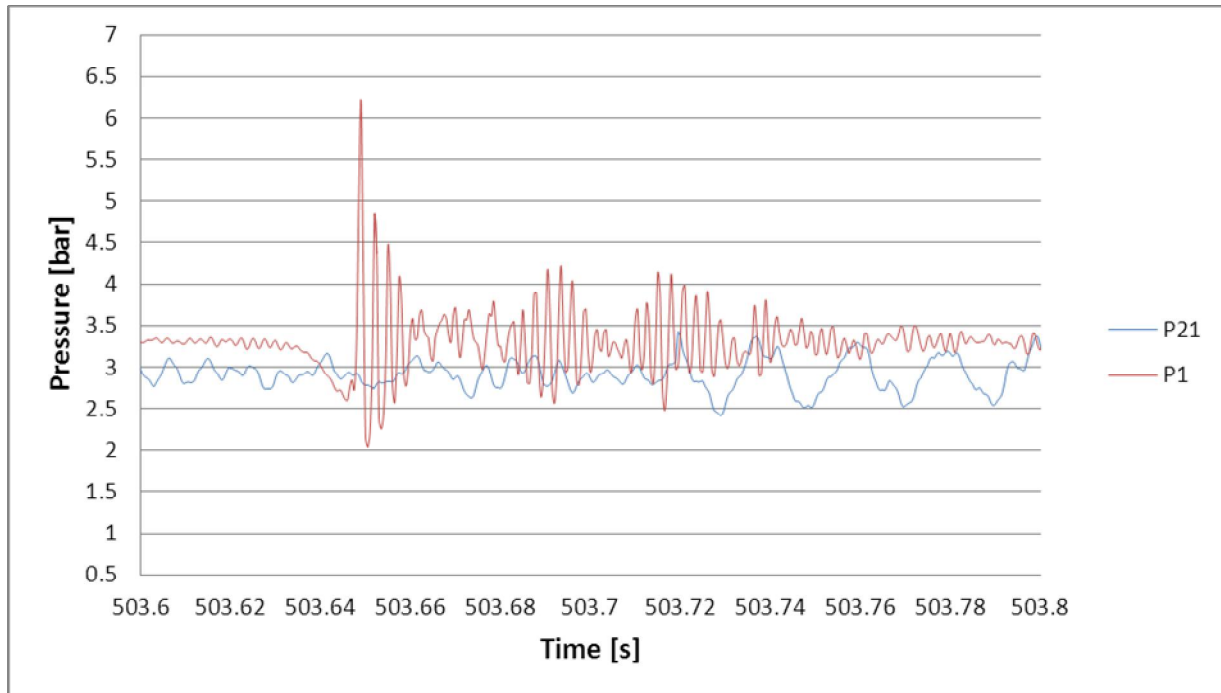


Figure 40. Example of a case where desynchronization time was not determined.

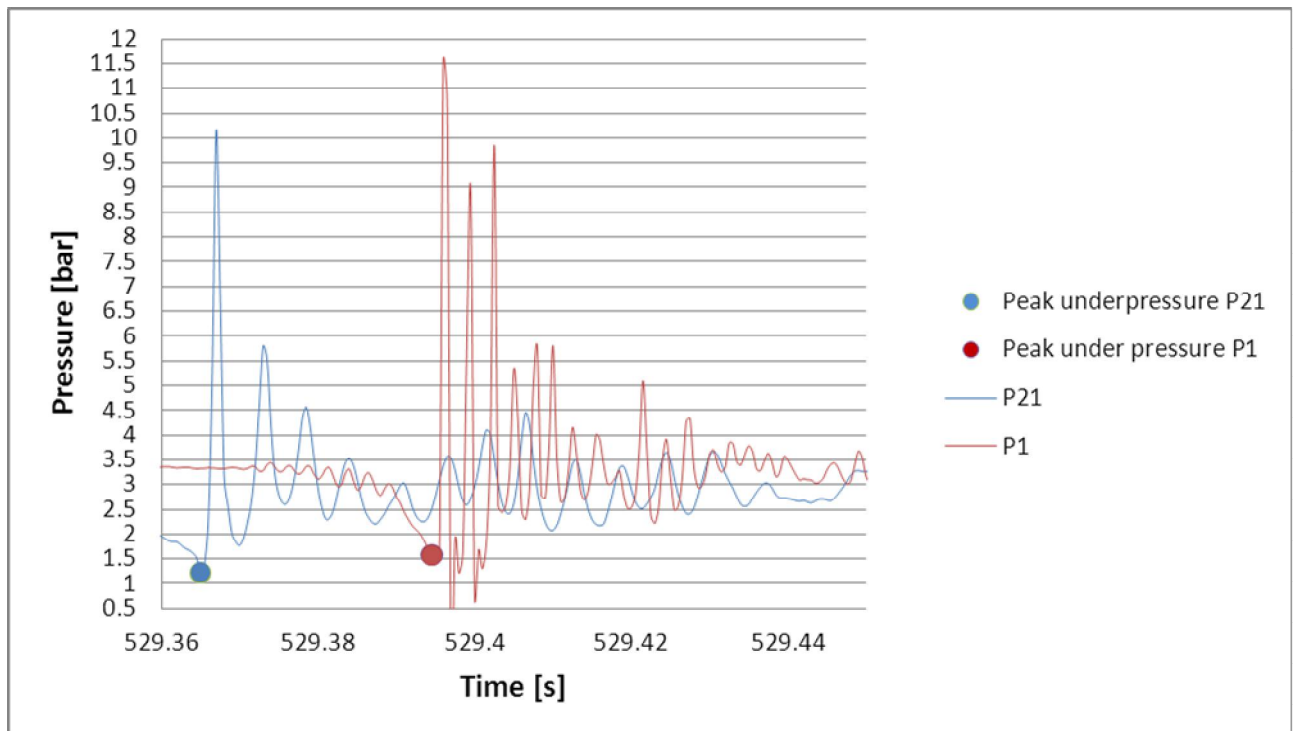


Figure 41. Example of a case where desynchronization time between chugging events could be determined. The blue and red dot indicate the time of peak under pressure.

In the end 120 pressure fluctuation events were determined from the time-pressure history of pipe 1 and 144 events from pipe 2. Out of these events 58 pairs of events were selected for the statistical determination of the desynchronization time.

The peak underpressure was assumed to represent the time of bubble collapse and therefore the desynchronization time of chugging was determined as the difference in time between peak under pressure occurrences of the two pipes. The desynchronization time in the case presented in Figure 41 would simply be:

$$\Delta t_{ds} = t_{p21} - t_{p1},$$

where  $\Delta t_{ds}$  is the desynchronization time,  $t_{p21}$  is the time of peak under pressure in pipe 2 and  $t_{p1}$  is the time of peak underpressure in pipe 1.

Figure 42 presents the desynchronization histogram. The desynchronization times are divided into 8 classes with same width. For instance the desynchronization time for six events ranged from -26.25 ms to -12.75 ms whereas 18+18 events occurred for which the desynchronization time varied between -12.75 ms and 14.25 ms. The standard deviation of desynchronization was determined to be 38 ms.

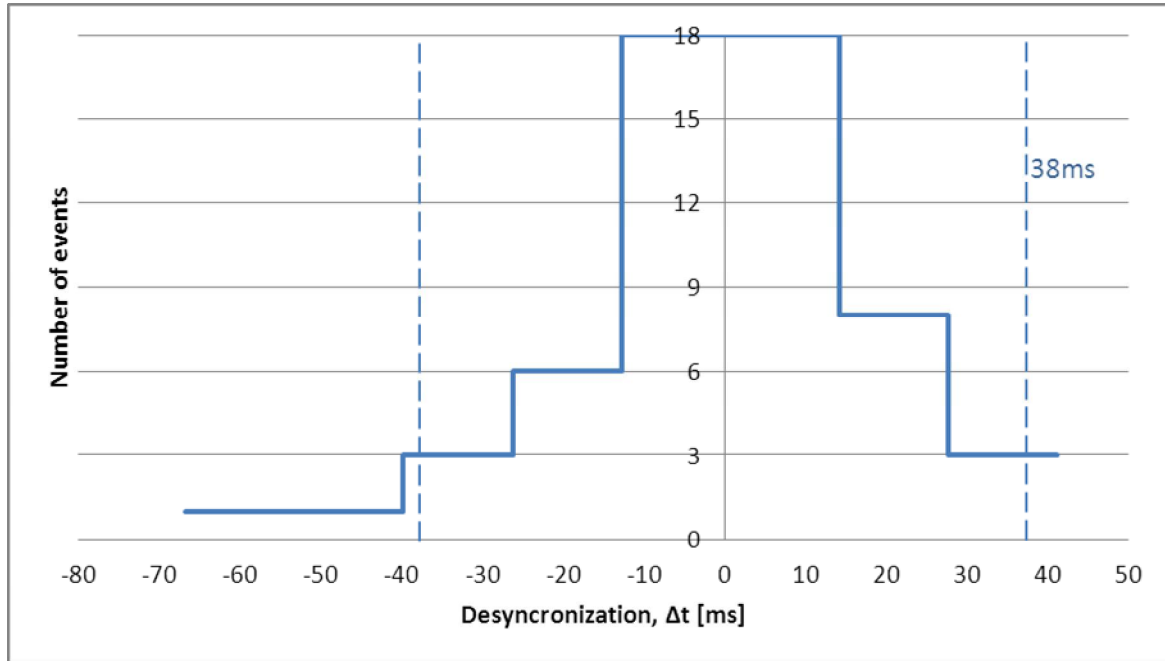


Figure 42. Histogram of desynchronization of time of peak underpressure.

### 4.3 Comparison between earlier experiments

Kukita and Namatame (1985) have studied the desynchronization in a full-sized seven-vent-system performed with JAERI test facility (Namatame et al., 1980). They analyzed altogether 980 chugging events from 23 test runs. In a seven-vent system a mean desynchronization time was determined for each chugging event. In this case chugging event consists of chugging in seven different pipes. The desynchronization time was then computed by determining the difference in time between individual chugging event and mean value. This differs somewhat from the desynchronization time definition used in this study. As only two pipes exist in experiment PAR-10, no mean value is computed and the desynchronization

time is the time difference between two peak under pressures. The standard deviation for all chug-events in the study performed by Kukita and Namatame (1985) was found to be 82 ms and for large chugs, for which the pool boundary load amplitude was larger than 10 kPa, the standard deviation was 42 ms. This is logical, since more synchronous chug events cause larger pool boundary loads. To make the standard deviation determined in this study comparable to the one obtained by Kukita and Namatame (1985), a mean time for each chugging event, consisting of chug-event at two pipes, was also determined and desynchronization was determined as time difference between mean value and individual chug-event. Hence the standard deviation for the desynchronization time in this study would be 13.6 ms, which is less than half of the standard deviation of large chugs in the seven-vent large-scale test. It seems logical that the desynchronization time is shorter for the smaller-scale PPOOLEX experiment. In the PPOOLEX facility, distance between the pipes is about 0.5 m, whereas in the JAERI facility the shortest distance is about 1.2 m and the longest about 4.7 m. The vent pipe diameters are about 0.2 m and 0.6 m for PPOOLEX and JAERI, respectively. Also the different number of pipes and different geometry may affect the desynchronization behaviour. Furthermore, it has to be kept in mind that the data from which Kukita and Namatame (1985) derived the results are from several different experiments with different test parameters.

## 5 Preliminary FEM calculations of chugging in a BWR containment

A finite element model of the whole containment was utilized in the attempt to model the effect of desynchronization. The analyses were carried out using implicit dynamic and modal dynamic analyses. The implicit dynamic analysis is expensive, since a set of non-linear dynamic equilibrium equations are solved at each time increment. The modal procedure (transient modal dynamic analysis in Abaqus) gives the response of the model as a function of time on a given time dependent loading (Abaqus, 2010). The response is based on a subset of the eigenmodes of the system, which are first computed. The modal amplitudes are integrated through time and the response is formed from the computed modal responses. In the case of linear systems, the modal dynamics procedure is less expensive than the direct integration of the entire system. The drawback of the modal dynamic procedure is that it does not support material damping in the case of coupled acoustic-structural analysis. Additionally, the sufficient number of eigenmodes to be extracted and used in the computation of the response of the structure is a matter of judgement on behalf of the users. Insufficient amount of computed eigenmodes will affect the accuracy of the computation.

### 5.1 Acoustic-structural analysis

The containment is meshed using 8-noded linear hexahedron elements, with reduced integration, whereas the upper and lower part of the water is meshed with acoustic 8-noded linear brick and 4-noded linear tetrahedron elements respectively. The number of modes to be computed and utilized and highest frequency of interest was set to 1000 Hz and 500 Hz respectively in the analyses using modal dynamics procedure. The relations of the sum of effective masses to the mass of the containment to x-, y- and z-directions were above 0.8 in all considered cases. At high mode numbers the effective masses were significantly



low compared to the mass of the containment, hence it was assumed that the number of extracted modes was sufficient. As mentioned in the report by Björndahl and Andersson (1998) the speed of sound in the water may vary from 450 m/s to 1280 m/s. This affects the acoustic pressure loading caused by chugging. Hence three different cases were considered where the speed of sound in water in case 1, case 2 and case 3 are 500 m/s, 1000 m/s and 1491 m/s respectively. In order to compare the effect of desynchronization, an analysis (case 4) where all the bubbles collapsed at the same time, was performed. The speed of sound in the water in case 4 was 1491 m/s and the analysis was performed with the modal dynamics procedure. The speed of sound in the water was adjusted by changing the bulk modulus of the water while keeping the water density constant. The finite element model of the containment is presented in Figure 43 and Figure 44 and the material properties in Table 3. Steel rebars are not included in the concrete and only upper part of the RPV contains steel, hence the material damping of steel is not of great importance. The Rayleigh damping for concrete with respect to frequency is presented in Figure 45.

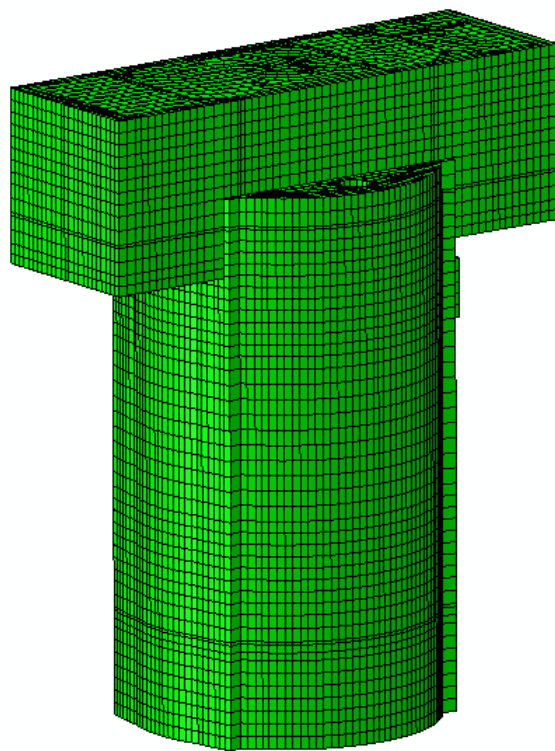


Figure 43. Finite element model of containment.

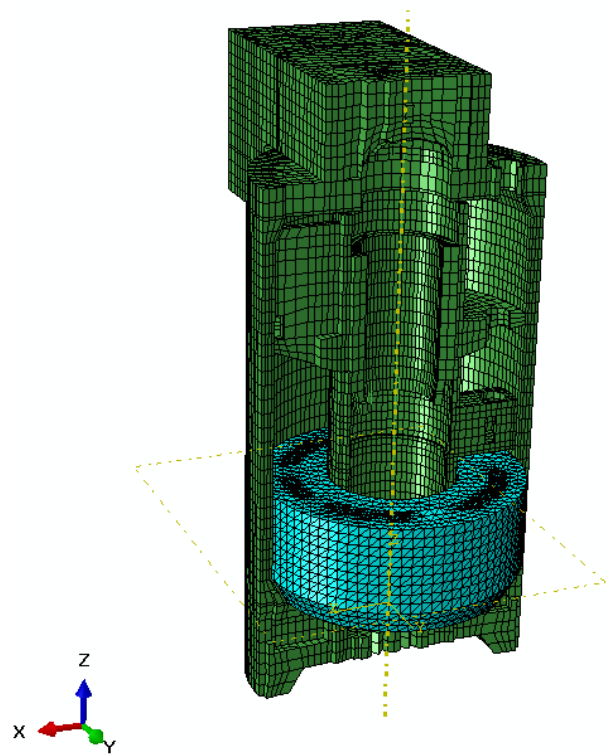


Figure 44. Cross-section of the finite element model.

Table 3. Material properties.

property	Concrete	Material Steel	Water
<b>Damping</b>			
Alpha	5.8900	4.7120	
Beta	9.9470E-05	7.9580E-05	
Composite	0	0	
Structural	0	0	
<b>Density [kg/m<sup>3</sup>]</b>	2 400	7 850	1 000
<b>Young's Modulus [MPa]</b>	39 000	200 000	
<b>Poisson's Ratio</b>	0.17	0.30	
<b>Bulk Modulus [Mpa]</b>			
<b>CASE1: speed of sound in water 500m/s</b>	-	-	250
<b>CASE2: speed of sound in water 1000m/s</b>	-	-	1000
<b>CASE3: speed of sound in water 1491m/s</b>	-	-	2 224
<b>CASE4: speed of sound in water 1491m/s</b>	-	-	2 224

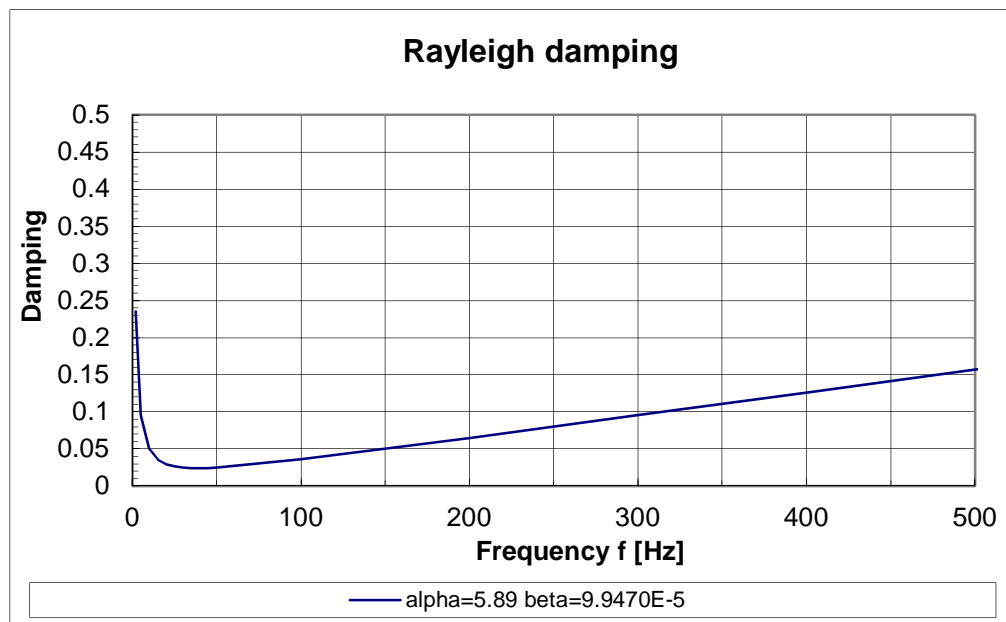


Figure 45. Rayleigh damping for concrete.

## 5.2 Load description

The loading in the finite element analyses is created as inward volume acceleration, as used and described in the previous studies by Pättikangas et al. (2011). There are sixteen blowdown pipes located at the BWR containment. An attempt was made to model the effect of desynchronization of chugging by determining the time of initiation for chugging for each pipe separately. The number and location of each pipe is presented in Figure 46.

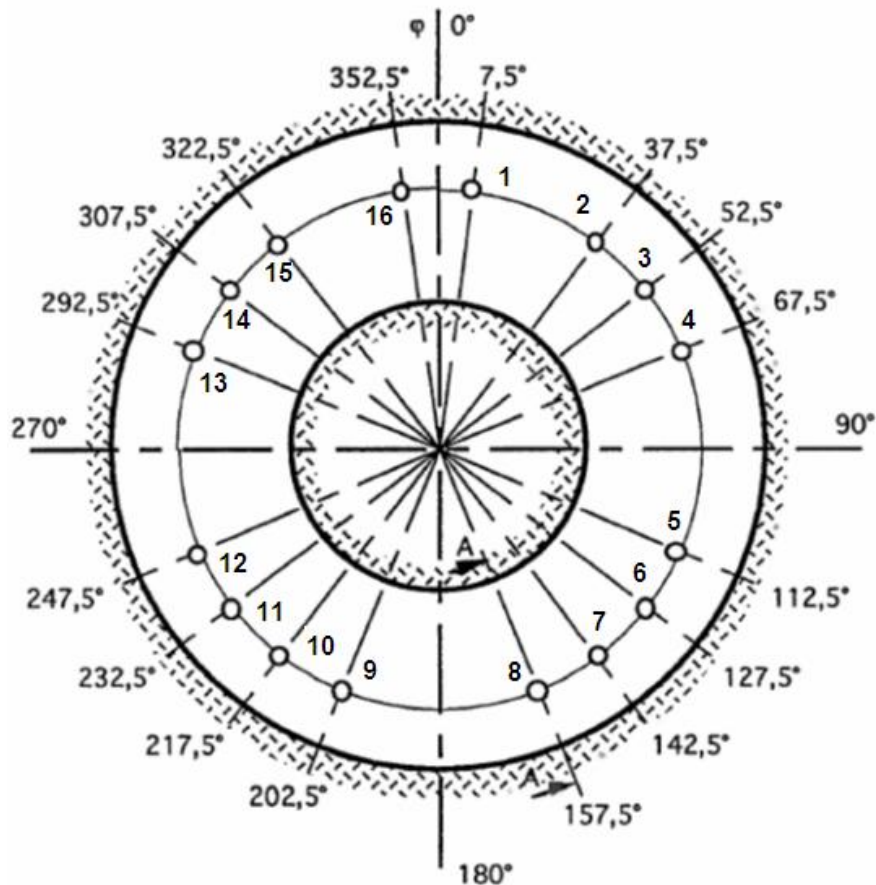


Figure 46. Location and numbering of the blowdown pipes.

The desynchronization time was taken into account by creating a normal distribution with mean value being zero and standard deviation 0.042 s as reported by Kukita and Namatame (1985) for large chugs in seven-vent large-scale test. The standard deviation determined by Kukita and Namatame (1985) was assumed to be more representative for BWR containment with 16 blowdown pipes, than the standard deviation of 0.038 s as determined in the two-vent pipe test PAR-10. Out of this distribution, sixteen initiation times were determined using Matlab's random-function, which gives randomly selected values out of given distribution. The normal distribution describing the desynchronization time and determined chugging initiation times are presented in Figure 47. The initiation times were then shifted so that the first chug event takes place at  $t = 0$  s.

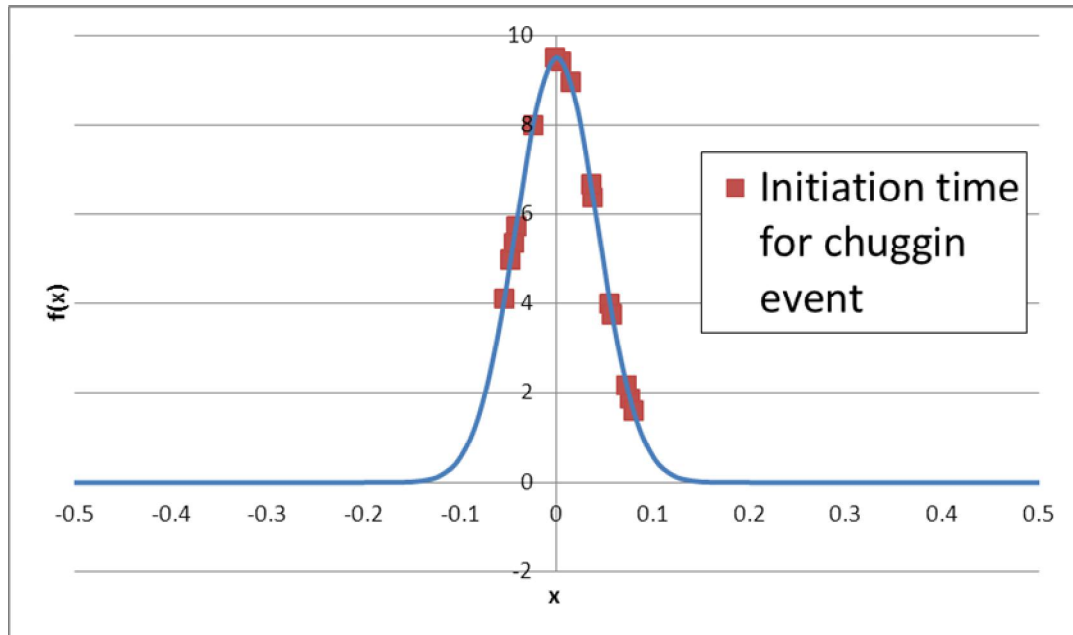


Figure 47. Normal distribution for desynchronization time and randomly selected initiation times.

The shape of the inward volume acceleration including the low-pressure phase was determined from a representative chug event in experiment COL-01, but the length was scaled up to match the length of a representative chug event in the seven-vent test reported by Kukita and Namatame (1985). In a single-vent test COL-01, the time from steady state to peak value was approximately 0.01 s, whereas in the seven-vent test the time corresponding to same event was approximately 0.15 s. Since the finite element model is linear, also the maximum amplitude was scaled down to one, in order to make further adjustments to the maximum load amplitude possible. For instance, if one was interested about the displacement in the containment with inward volume acceleration amplitude  $p$ , one would only have to multiply the displacement values obtained with the current model by the factor  $p$ . The scaled inward volume acceleration for individual chugging event is presented in Figure 48. The times of initiation and inward volume acceleration for 16 bubbles forming at 16 different pipes are presented in Figure 49.

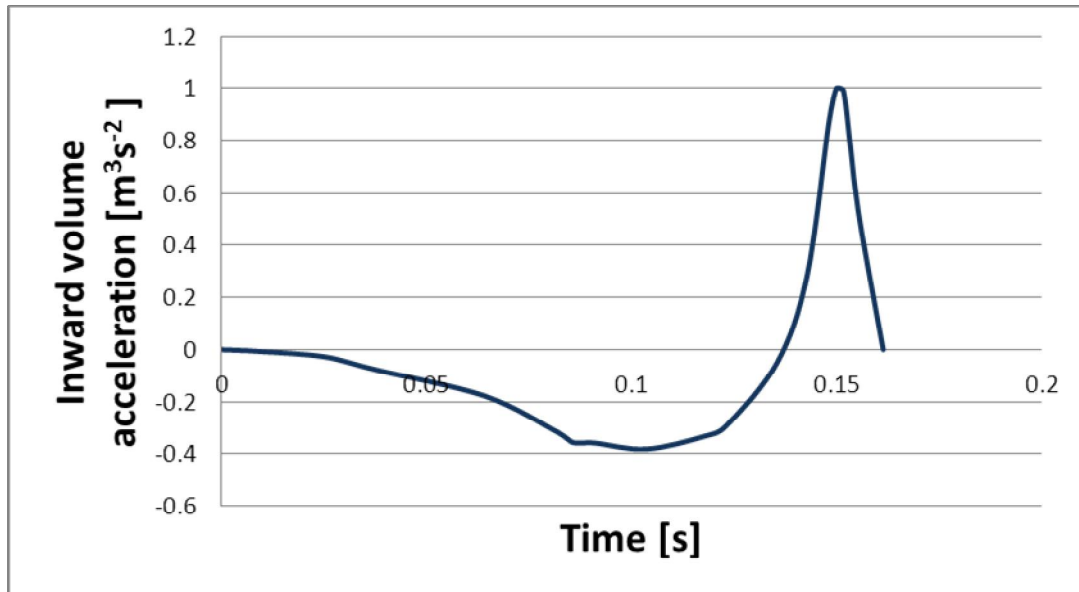


Figure 48. Volume acceleration for bubble collapses.

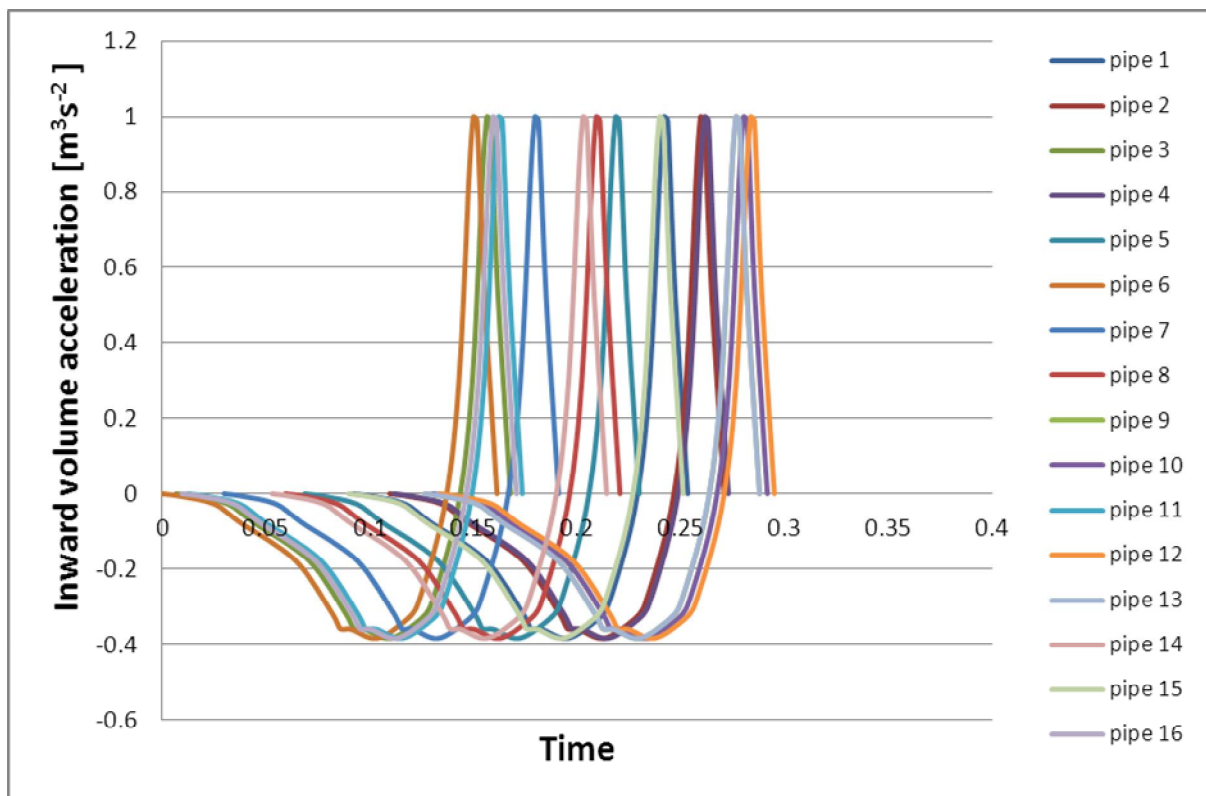


Figure 49. Inward volume acceleration and time of initiation for all 16 pipes.

### 5.3 Results and discussion

The maximum von Mises stresses for each case are presented in Table 4.

*Table 4. Maximum von Mises stresses. Note that the normalized loading has been used and the absolute values are hence not realistic.*

Analysis type	CASE	maximum von Mises stress [Pa]
modal	1	3064
implicit	1	2233
modal	2	2718
implicit	2	2047
modal	3	3462
implicit	3	2566
modal	4	7061

Maximum von Mises stresses at the wet well wall and their time of occurrences in cases 1, 2 and 3 are presented again in Figure 50, where also the inward volume accelerations of the bubbles are reshown. The dark blue, red and grey markers present the results obtained from analysis where the speed of sound in the water is 500 m/s, 1000 m/s and 1491 m/s, respectively. The stresses obtained from implicit analysis procedure are presented with round markers and the results from modal dynamics procedure with square shaped markers.

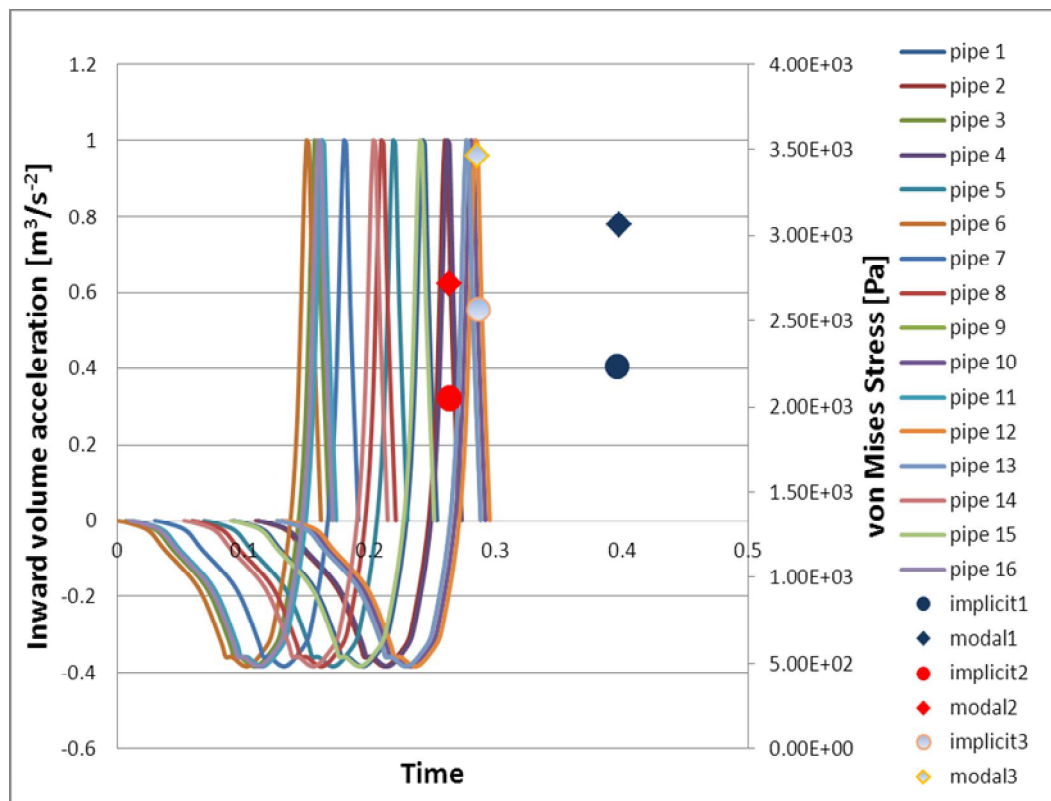


*Figure 50. Maximum von Mises stresses at the wet well wall and loading with respect to time.*

It is seen that the time and magnitude of maximum stress varies from one analysis to another. The stresses are higher in the analyses performed with modal



dynamics procedure, which is assumed to result from the absence of material damping, but was not verified in this study. As the speed of sound in the water was altered, also the time of occurrence, location and magnitude of maximum von Mises stress changed. The locations where the maximum von Mises stress occurred were not altered by chosen analysis method and are presented in relation to pipe locations in Figure 51 to Figure 53. The pictures present a horizontal cut-through from the containment above the water level of wet well. The locations pointed out with red arrows are not in the plane of the figure, but are located under the water surface. In cases 2 and 3 the location of occurrence of maximum von Mises stresses can be explained by comparing the location in relation to pipe positions and the time of initiation of chugging for each pipe presented in Figure 50. In case 3, chugging has taken place in pipes 9, 10, 12 and 13 before the maximum stress occurred. Respectively, in case 2, chugging has taken place in pipes 2 and 4 just before the occurrence of maximum stress. Loading in pipes 2 and 4 are most synchronized, the time difference between amplitudes being only 0.002 s. The distance between the pipes and the speed of sound play a role here. Regardless of the longer distance, apparently bubble collapse taking place at pipes 9 and 13 contribute to the loading experienced by the element where the maximum stress occurs due to the higher speed of sound in case 3. In case 1, the maximum value does not occur simultaneously with any chugging event. Because the speed of sound in water in this case was only 500 m/s, the structures response is not as immediate as in the case of higher speed of sound, the location and time of occurrence becomes harder to explain and to predict. Vertical cross-section of the lower part of the containment is presented in Figure 54, where deformation (multiplied by  $1.7 \cdot 10^6$ ) at the pool boundary in case 3 at the time of occurrence of maximum von Mises stress can be observed. The outer wall has bulged due to the pressure wave, causing compression at the inner side of the wall and correspondingly tension at the outer side of the wall.

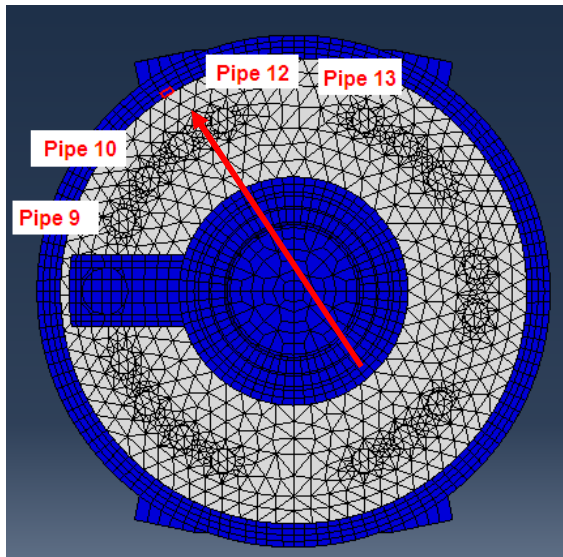


Figure 51. Location of maximum von Mises stress in relation to pipes in case 1.

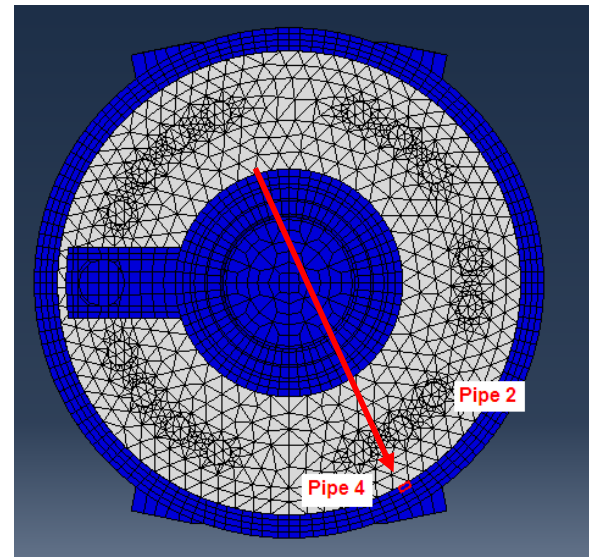


Figure 52. Location of maximum von Mises stress in relation to pipes in case 2.

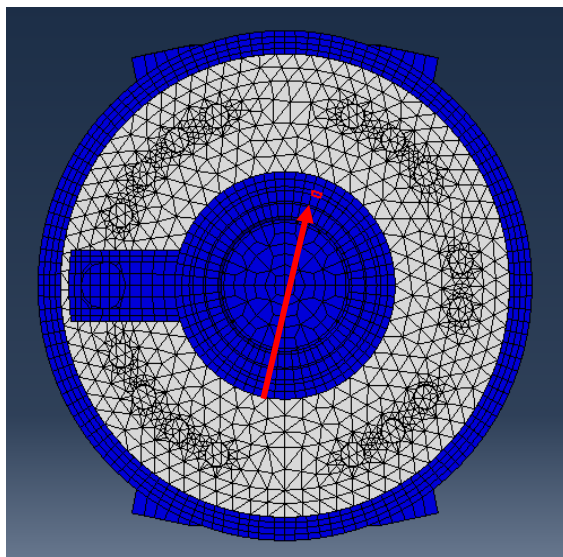


Figure 53. Location of maximum von Mises stress in relation to pipes, in case 3.

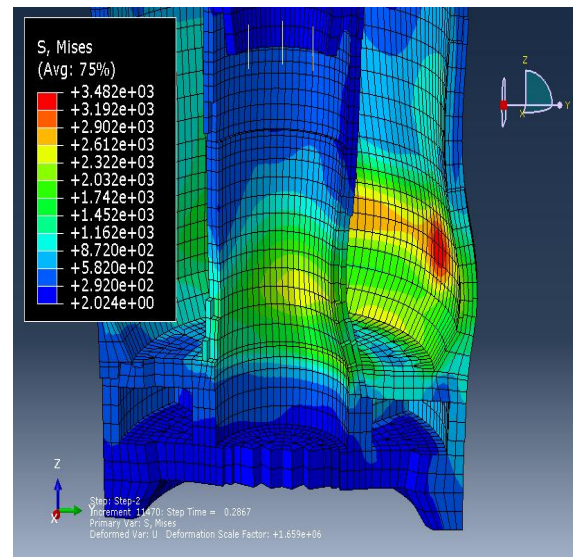


Figure 54. Vertical cross-section of the containment at the time of occurrence of maximum von Mises stresses at the pool boundary in case 1.

The maximum von Mises stresses in a case where chugging took place simultaneously in all pipes was over 0.007 MPa whereas maximum of all analysis utilizing desynchronization was found in case 3 using modal dynamics procedure, maximum von Mises stress being approximately 0.0035 MPa. It must be pointed out again that the absolute values of the stresses are not realistic since the normalized loading has been used. In both cases the speed of sound is 1491 m/s. Thus the maximum stress in the case where desynchronization was considered was

less than half of the corresponding value in an analysis where chugging took place simultaneously in all pipes. Both analyses assume that the amplitude of the inward volume acceleration is same for all pipes. However measured pressures in tests with multiple blowdown pipes indicate non-uniform amplitudes. This implies that in addition to considering desynchronization, also variance in the source strength might have to be considered. Even though the desynchronization was considered in cases 1 - 3, it was considered to be similar in all cases. In order to get more realistic picture of the effects of desynchronization, more analyses with desynchronization time varying randomly in a given distribution should be considered. By verifying the responses given by the modal dynamics procedure, the analysis times can be decreased considerably.

## 6 Discussion

The CFD simulation performed for the PPOOLEX experiment PAR-10 show some clear differences compared to the experiment. In the simulation, the period of chugging is much shorter than in the experiment. The period in the simulation is about 0.7 s and in the experiment about 1.7 s. In spite of the changes done in the modeling, the condensation seems to be too weak. In the experiment, all the condensation occurs near the outlet of the vent pipe or inside the vent pipe. On the contrary, in the simulation some condensation occurs in the vapor plume rising upwards from the vent outlet.

The differences between the simulation and the experiment are probably caused by three main reasons. First, the heat transfer coefficient between liquid water and vapor may still be too small. Second, the interfacial area estimated from the gradient of the void fraction is probably too small. The product of the heat transfer coefficient and the interfacial area determine the condensation rate, and it is difficult to distinguish their roles in the experimental result. Third, one can see in the experiment that mixing is rapidly increased on the interface of the vapor bubble when it starts collapsing at the vent outlet. The role of this increased mixing is still not properly taken into account in the present numerical model.

The rapid collapse of a steam bubble was analyzed with the new Eulerian model of Abaqus. Bubble collapses giving the largest pressure loads in the PPOOLEX experiment COL-01 were analyzed and the computational results were compared with the experiment. Pressure pulse calculated by using an axisymmetric model became clearly too high and narrow, even though the collapse time was correct. There are several possible reasons for the low and wide experimental pressure peaks, which were briefly discussed. Although the calculations could not predict the over-pressure peaks correctly, they may be suitable for fitting the pressure variation inside the bubble to the experimentally observed under-pressure signal near the bubble. In this work, constant, linear and quadratic pressure variations were tested and fitted to the experimental data. The linear and quadratic pressure variations produced fairly realistic results; overall, the linear case was in better agreement with the experiments. The pressure variation inside the bubble can be used for estimating the condensation rate of steam in future. In addition to calculating the PPOOLEX experiment, effect of various parameters, such as the system size, on the pressure peak were examined for the spherical and toroidal bubbles. Results of these parametric studies can be used for studying more thoroughly the scaling of the experimental results to full-scale in future.

The desynchronization of chugging events in the two vent experiment PAR-10 was studied. Statistical distribution of desynchronization was determined from the measured pressure data and compared to results obtained in a seven vent pipe experiment found from literature. The standard deviation of the desynchronization times was found to be 38 ms in this experiment.

The response of BWR containment during desynchronized chugging events and with varying speeds of sound was numerically computed using direct time integration and modal dynamics procedure available in Abaqus.

Desynchronization between chugging events was taken into account by determining individual time of initiation of chugging for each pipe. Normal distribution with zero mean value and standard deviation of 42 ms was created and out of this distribution sixteen initiation times were determined using a random-function. The shape of the inward volume acceleration was determined from a representative chug event in single-vent experiment COL-01, but the length was scaled up to match the length of a representative chug event in the seven-vent large-scale test found from literature. Stresses obtained using modal dynamics procedure were found to be higher than those obtained using direct time integration which is assumed to result from the absence of damping in modal dynamics procedure, but this was not verified in this study. In addition to time and magnitude, also the location of maximum stresses changed with speed of sound. When desynchronization was taken into account, highest stresses were obtained with highest speed of sound. Preliminary results with modal superposition procedure show significant decrease in the loads experienced by the containment, when the desynchronization is taken into account. In order to get more realistic picture of the effects of desynchronization, more analyses with desynchronization time varying randomly in a given distribution could be considered.

## References

- Abaqus, 2010. Analysis User's Manual, Dassault Systèmes, Providence, RI, Version 6.10-2.
- Abaqus, 2011. Analysis User's Manual, Dassault Systèmes, Providence, RI, Version 6.11-1.
- Banerjee, S., 1978. A surface renewal model for interfacial heat and mass transfer in transient two-phase flow, *International Journal of Multiphase Flow* **4**, 571 - 573.
- Björndahl, O. and Andersson, M., 1998. Globala vibrationer vid kondensationsförlopp i wetwell orsakade av LOCA i BWR-anläggningar. Swedish Nuclear Power Inspectorate, SKI Report 99:3, Stockholm, 81p.
- Coste, P., Pouvreau, J., Laviéle, J. and Boucker, M., 2008. A two-phase CFD approach to the PTS problem evaluated on COSI experiment, *Proc. 16<sup>th</sup> Int. Conf. on Nuclear Engineering ICONE16*, Orlando, FL, USA, May 11–15, 2008.
- Giencke, E., 1981. Pressure distribution due to a steam bubble collapse in a BWR pressure suppression pool. *Nuclear Engineering and Design* **65**, 175 - 196.
- Hughes, E.D., and Duffey, R.B., 1991. Direct contact condensation and momentum transfer in turbulent separated flows. *International Journal of Multiphase Flows* **17**, 599.
- Kukita, Y. and Namatame, K., 1985. The vent-to-vent desynchronization effects on LOCA steam condensation loads in BWR pressure suppression pool. *Nuclear Engineering and Design* **85**, 141 - 150.
- Lahey, R.T., Jr. and Moody, F.J., 1993. The thermal-hydraulics of a boiling water nuclear reactor, 2<sup>nd</sup> edition, American Nuclear Society, USA.
- Laine, J., Puustinen, M. and Räsänen, A., 2009. PPOOLEX experiments with a modified blowdown pipe outlet. Lappeenranta University of Technology, Nuclear Safety Research Unit, Research report CONDEX 2/2008, 29 p. + app. 8 p.
- McCauley, E.W., Holman, G.S., Aust, E., Schwan, H., Vollbrandt, J. and Fürst, H., 1981. Description of steam condensation phenomena during the loss-of-coolant accident. 6<sup>th</sup> International Conference on Structural Mechanics in Reactor Technology, Vol. B, Paris, France, August 17 - 21, 1981.
- Namatame, K. et al., 1980. Full-Scale Mark II CRT Program: facility description, Japan Atomic Energy Research Inst., JAERI-M 8780.
- Puustinen, M., 2006. Combined effects experiments with the condensation pool test facility. Lappeenranta University of Technology, Nuclear Safety Research Unit, Research report POOLEX 1/2006, 30 p. + app. 6 p.

Puustinen, M., Laine, J. and Räsänen, A., 2010. PPOOLEX experiments on dynamic loading with pressure feedback, Lappeenranta University of Technology, Nuclear Safety Research Unit, Research report CONDEX 2/2009, 42 p.

Puustinen, M., Laine, J. and Räsänen, A., 2011. Multiple blowdown pipe experiments with the PPOOLEX facility. Lappeenranta University of Technology, Nuclear Safety Research Unit, Research Report CONDEX 2/2010, 28 p. + app.8 p.

Pättikangas, T., Niemi, J. and Timperi, A., 2011. Numerical modelling of pressure suppression pools with CFD and FEM codes. VTT Technical Research Centre of Finland, Research Report VTT-R-00927-11, Espoo, Finland, 53 p.

Štrubelj, L. Ézsöl, G. and Tiselj, I., 2010. Direct contact condensation induced transition from stratified to slug flow, Nuclear Engineering and Design **240**, 266 - 274.

Tanskanen, V., Lakehal, D. and Puustinen, M., 2008. Validation of direct contact condensation CFD models against condensation pool experiment, Workshop on Experiments and CFD Code Application to Nuclear Reactor Safety (XCFD4NRS), Grenoble, France, 10–12 September, 2008, 12 p.



Title	Modeling of interaction of multiple vent pipes in a pressure suppression pool
Author(s)	Antti Timperi, Michael Chauhan, Timo Pättikangas and Jarto Niemi
Affiliation(s)	VTT- Technical Research Centre of Finland
ISBN	978-87-7893-337-9
Date	April 2012
Project	NKS-R / ENPOOL
No. of pages	54
No. of tables	4
No. of illustrations	54
No. of references	18
Abstract	<p>Calculations of direct-contact condensation in the pressure suppression pool have been performed. Partial pressure model for the condensation of pure vapor is used for the condensation, which makes possible modeling of the condensation of pure vapor. The heat and mass transfer during condensation is studied in detail for experiment PAR-10 in the PPOOLEX facility.</p> <p>The rapid collapse of a steam bubble in PPOOLEX experiment COL-01 has been analyzed with the new Eulerian model of Abaqus. By observing the collapse behavior, the pressure variation inside the bubble was fitted with the experiment. The effect of system size on the pressure peak was also examined; these results can be used for studying more thoroughly the scaling of the experimental results to full-scale in future.</p> <p>The desynchronization of chugging events in the two vent experiment PAR-10 was studied. The statistical distribution of desynchronization was determined from the measured pressure data and compared to results obtained in a seven vent pipe experiment found from literature. The response of BWR containment during desynchronized chugging events and with varying speeds of sound was numerically computed using direct time integration and modal dynamics procedure available in Abaqus.</p>
Key words	Condensation pool, pressure suppression pool, BWR, CFD, fluid-structure interaction, FSI